



The Challenge of CO Hydrogenation to Methanol: Fundamental Limitations Imposed by Linear Scaling Relations

Elnabawy, Ahmed O.; Schumann, Julia; Bothra, Pallavi; Cao, Ang; Nørskov, Jens K.

Published in:
Topics in catalysis

Link to article, DOI:
[10.1007/s11244-020-01283-2](https://doi.org/10.1007/s11244-020-01283-2)

Publication date:
2020

Document Version
Peer reviewed version

[Link back to DTU Orbit](#)

Citation (APA):
Elnabawy, A. O., Schumann, J., Bothra, P., Cao, A., & Nørskov, J. K. (2020). The Challenge of CO Hydrogenation to Methanol: Fundamental Limitations Imposed by Linear Scaling Relations. *Topics in catalysis*, 63, 635–648. <https://doi.org/10.1007/s11244-020-01283-2>

General rights

Copyright and moral rights for the publications made accessible in the public portal are retained by the authors and/or other copyright owners and it is a condition of accessing publications that users recognise and abide by the legal requirements associated with these rights.

- Users may download and print one copy of any publication from the public portal for the purpose of private study or research.
- You may not further distribute the material or use it for any profit-making activity or commercial gain
- You may freely distribute the URL identifying the publication in the public portal

If you believe that this document breaches copyright please contact us providing details, and we will remove access to the work immediately and investigate your claim.

The Challenge of CO Hydrogenation to Methanol: Fundamental Limitations Imposed By Linear Scaling Relations

Ahmed O. Elnabawy¹, Julia Schumann², Pallavi Bothra³, Ang Cao¹, Jens K. Nørskov^{1*}

¹Department of Physics, Technical University of Denmark, Lyngby DK-2800, Denmark

²Current address: Department of Physics and Astronomy, University College London, London, United Kingdom; Department of Chemical Engineering, University College London, London, United Kingdom

³Current address: Department of Chemical and Biomolecular Engineering, Los Angeles, CA 90024, United States

Corresponding author: Jens K. Nørskov. E-mail: jkno@dtu.dk

ORCID:

Ahmed O. Elnabawy: 0000-0002-8911-1916

Julia Schumann: 0000-0002-4041-0165

Abstract

Recent developments in computational catalysis have allowed the routine reduction of the dimensionality of complex reaction networks to a few descriptors based on linear scaling relations. Despite this convenient benefit, linear scaling relations fundamentally limit the activity and selectivity of a given class of materials towards a given reaction. Here, we show an example by offering a novel description of the fundamental limits on the activity of CO hydrogenation to methanol; a reaction that offers a sustainable route to obtaining value-added chemicals from syngas. First, we show that there is a strong linear correlation between the formation energy of CO* (where * denotes an adsorbed species) and those of the transition states of a number of elementary steps along the methanol synthesis pathway on these surfaces. Using microkinetic modeling, we cast this information into activity volcano plots with the formation energies of a given transition state and CO* as independent descriptors. This analysis reveals the fundamental limits on activity imposed by the aforementioned linear scaling relations, and invites a vigorous search for novel materials that escape these linear scaling relations as a necessary condition for achieving improved activity towards methanol from CO hydrogenation. Specifically, we point out the transition states H-CO* and CH₃O-H* as key transition states to be stabilized independently of CO* for improved activity and selectivity towards methanol synthesis.

Keywords: methanol synthesis, density functional theory, linear scaling relations, catalyst design, microkinetic modeling

1 Introduction

There is a general scientific consensus that global warming is driven by anthropogenic emissions caused by our current energy infrastructure which releases the carbon fixated in fossil fuels into the atmosphere as CO₂ [1]. To mitigate this crisis, fossil fuels must be replaced by more sustainable fuels that can be produced from CO₂ directly or indirectly (e.g. through biomass) [2,3]. Methanol is a convenient basis fuel molecule [4-7], a liquid at ambient conditions, a hydrogen carrier [8], a feed to direct methanol fuel cells [9], a blend to gasoline in combustion engines [8], and a platform molecule for the production of gasoline, diesel, jet fuel, or higher value chemicals [10,11]. Today, methanol is industrially produced from syngas – a mixture of predominantly CO and H₂ with 2-8 vol% of CO₂ – on a Cu/ZnO/Al₂O₃ catalyst at 30-120 atm and 200-300 °C [7,12-14]. In a descending order of molar amounts, Cu represents the active component of the catalyst, ZnO modifies and disperses Cu in porous aggregates partially covered by Zn or ZnO, while Al₂O₃ plays the role of a structural promoter [15-25]. A strong metal support interaction (SMSI) effect brings about a much-prized synergy in this catalytic system, by partially covering the Cu surface with Zn/ZnO, which strongly stabilizes crucial intermediates and transition states along the hydrogenation pathway (particularly of that of CO₂) [26-29]. Despite this synergistic collection of the catalyst components, turnover frequencies for methanol synthesis from syngas often do not exceed an unimpressive 10⁻² s⁻¹ [26,30-33]. This rate is much lower than that of the intimately intertwined water-gas-shift-reaction, allowing the interconversion between CO and CO₂ to equilibrate under the industrial conditions of methanol synthesis [34].

Density functional theory (DFT) is well positioned to contribute to advancements in catalysis thanks to the ever-growing computational capabilities and increasing accuracy of exchange correlation functionals [35-38]. In the context of methanol synthesis from syngas, DFT has provided much insight into the mechanism and structure-sensitivity on transition metal catalysts [26,29,39-50]. Extensive calculations for the adsorption energies of reaction intermediates and the transition state

energies for the various elementary steps paint a fairly complete picture of the energetics of the involved reaction networks on a given surface. By repeating this exercise on a number of structurally similar surfaces, one can elucidate trends among those surfaces for CO hydrogenation to methanol. One approach to understanding these trends and equipping them with a predictive capability is to reduce the dimensionality of the reaction network to a few descriptors through linear scaling relations between those few chosen descriptors and the remainder of the calculated energies [51]. For CO/CO₂ hydrogenation to methanol, the descriptors have consistently been the adsorption energies of CO* (or atomic carbon) and OH* (or atomic oxygen). Note that these two descriptors correlate poorly with each other on the terraces and steps of transition metals [43,52], and therefore both are needed as independent descriptors to fully characterize the reaction network. Through microkinetic modeling, the full energetics of the reaction network can be cast as a function of these two descriptors into two-dimensional volcano plots, showing regions in the descriptor space of improved activity and selectivity towards methanol, thus enabling rational catalyst design and high-throughput screening of catalytic materials.

In this work, we focus on the hydrogenation of CO, as opposed to the less plentiful component of syngas, CO₂. It is a common industrial practice to inject CO₂ into syngas [53], but the concentration of CO₂ is limited by its tendency to deactivate the industrial Cu/ZnO/Al₂O₃ catalyst through a combined poisoning (e.g. by water, the product of CO₂ hydrogenation) and sintering effect [54-58]. The general consensus is that CO₂ provides the active pathway to methanol formation on the industrial Cu/ZnO/Al₂O₃ catalyst, and that it is replenished in the syngas mixture through the continuous conversion of CO to CO₂ via the water-gas-shift-reaction [29,42,59-62]. Crucially, this chemical equilibrium removes the H₂O produced by CO₂ hydrogenation, which otherwise would have poisoned the surface (e.g. through high coverage of OH* or other oxygenated species). The elimination of this poisoning/deactivation problem, and funneling the methanol synthesis rate through

CO (i.e. the majority carbon source in syngas) as opposed to CO₂ necessitate finding catalysts that are active towards methanol synthesis primarily through CO hydrogenation, hence the focus of this work.

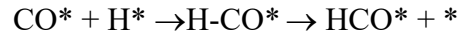
On the terraces and steps of Cu, the hydrogenation pathway of CO predominantly proceeds through the full hydrogenation of the carbon end of CO* to methoxy (CH₃O*), followed by the hydrogenation of the oxygen end to finally produce methanol (CH₃OH) [39]. Possible rate-determining steps include the initial hydrogenation of adsorbed CO* to HCO*, as well as the final hydrogenation of methoxy (CH₃O*) to methanol [39]. The initial hydrogenation step in particular has also been suggested as rate-determining for syngas conversion to higher alcohols [52]. Here, we seek a more in-depth perspective into the reaction mechanism by first focusing on this initial hydrogenation rate-determining step. We conduct our analysis on Ag, Cu, Pt, Pd, and Rh, a suitable set of transition metals that covers a wide range of adsorption properties. Given the strong structure sensitivity of methanol synthesis on Cu and the importance of steps in the industrial catalyst [16,26,30-32,63], we investigate the (111) and (211) facets of the aforementioned transition metals, to represent terraces and steps, respectively. We show that there exists a strong linear scaling relation between the energy of the initial state and that of the transition state for this elementary step. We then recast the microkinetic model to superimpose this linear scaling relation onto the two-dimensional volcano plots. We further explore other transition states along the CO hydrogenation to methanol pathway as descriptors for methanol synthesis on the (211) surfaces. This shows how this family of linear scaling fundamentally limits the activity of transition metals towards methanol synthesis from CO. We then proceed with a brief discussion of materials or strategies to escape these linear scaling relations.

2 Methods

DFT data on the (111) surfaces are taken from our previous work [52], while DFT data on the (211) surfaces were computed anew (see Table S1) on (211) slab models identical to our previous work [43]. Briefly, all plane wave DFT calculations presented here were performed as implemented in the Quantum Espresso code [64], with the BEEF-vdW functional [65] which accounts for van der Waals dispersions in the framework of the generalized gradient approximation. The (111) surfaces were modeled with a four-layer slab in a (3x3) unit cell, with the bottom two layers fixed while the top two layers and adsorbates were allowed to fully relax. The (211) surfaces were modeled using a (3x1) supercell structure with three metal layers, with the bottom two fixed and the upper layer and adsorbates fully relaxed. For both facets, the Brillouin zone was sampled with a 4x4x1 Monkhorst-Pack mesh [66], and the energy cutoff was taken at 500 eV. Transition states were calculated with the climbing image nudged elastic band (CI-NEB) method [67], with the convergence criterion on the forces on each of the five intermediate images of 0.05 eV/Å. The harmonic approximation was used to calculate vibrational frequencies and estimate zero-point energies and entropies. All transition states have a single imaginary frequency. Steady state solutions for the rate equations were obtained using the mean-field approximation as implemented in the CatMap code [68]; we employ our previous microkinetic models for the (111) [52] and (211) [43] surfaces. Methanol, methane, ethanol, and acetaldehyde are included as possible products on the (111) surfaces, while C₂ species were not included on the less C₂-oxygenates-selective (211) surfaces. C-O bond scission to form methane was considered through a COH*-like intermediate on the (211) surfaces, and through CHOH* on the (111) surfaces. All microkinetic models are solved at 523 K and 20 bar, with the reaction feed containing CO:H₂ ratio of 1:2, and negligible amounts of products (methane, methanol, and C₂ species if applicable). Formation energies of all species are relative to gas phase energies of CO, H₂, and H₂O.

3 Results

A common rate-determining step for CO hydrogenation to methanol is:



where * denotes an adsorbed species or a surface site, and H-CO* is the transition state for this association step, which determines the overall rate of the hydrogenation reaction. A general rate expression for this elementary step could be given as:

$$r = \nu\theta e^{-(G_{TS}-\Delta G)/kT}$$

where ν is the pre-exponential factor, θ is a generic term for the coverage of adsorbed intermediates of the initial state (CO* and H*), G_{TS} is the free energy of the transition state H-CO*, ΔG is the free energy of the initial state consisting of CO* and H*, k is the Boltzmann constant, and T is the absolute temperature.

The generic coverage term could in turn be related to reactant gaseous mixture pressure p by:

$$\theta = \frac{pK}{1 + pK}$$

where K is the equilibrium constant for the adsorption elementary steps, and is given by:

$$K = e^{-\Delta G/kT}$$

Combining the above equations, and setting p to unity gives the following form of the rate expression:

$$r = \nu \frac{1}{1 + e^{\Delta G/kT}} e^{-(G_{TS}-\Delta G)/kT}$$

We then simplify this expression further by considering two limiting scenarios for ΔG : a scenario for strongly adsorbing, highly covered surfaces ($\Delta G \ll 0$), and another for weakly adsorbing, clean surfaces ($\Delta G \gg 0$).

For $\Delta G \ll 0$, the above rate expression could be simplified to:

$$r \propto e^{-(G_{TS}-\Delta G)/kT} \approx e^{-(E_{TS}-\Delta E)/kT}$$

Notice that in the expression above we refer to the zero-point energy (ZPE)-corrected total energies instead of free energies. This follows by assuming a negligible change in entropy from the initial state to the transition state, a valid assumption given that both are adsorbed states.

As for $\Delta G \gg 0$, the above rate expression could be simplified to:

$$r \propto e^{-G_{TS}/kT} = e^{\Delta S_{TS}/k} e^{-E_{TS}/kT}$$

Given that $r \propto e^{-E_a/kT}$, we find that the expressions for the activation energies for the two limiting cases become:

$$\Delta G \ll 0 \quad , \quad E_a = E_{TS} - \Delta E \quad | \quad \Delta G \gg 0 \quad , \quad E_a = E_{TS}$$

That is to say that the activation energy equals the transition state energy if adsorption (i.e. the initial state) is uphill, but equals the difference between the transition state and initial state if the latter is downhill compared to the gas-phase reference.

For hydrogenation/dehydrogenation elementary steps, the transition state energy has been found to scale linearly with the energy of the dehydrogenated state [39,69]. Fig. 1 shows a strong linear scaling relation ($R^2 > 0.99$) between the transition state (E_{TS}) and the initial state (ΔE) of CO* hydrogenation to HCO* for the close-packed (111) and the stepped (211) facets of Ag, Cu, Pt, Pd, and Rh. The transition state is significantly stabilized on the (211) facets as compared to their (111) counterparts. Notice that the slopes for the two lines are quite similar; the two lines are solely distinguished through their intercepts, with the line for the (211) facets showing on average ~ 0.30 eV stabilization for H-CO* compared to the line for (111) facets.

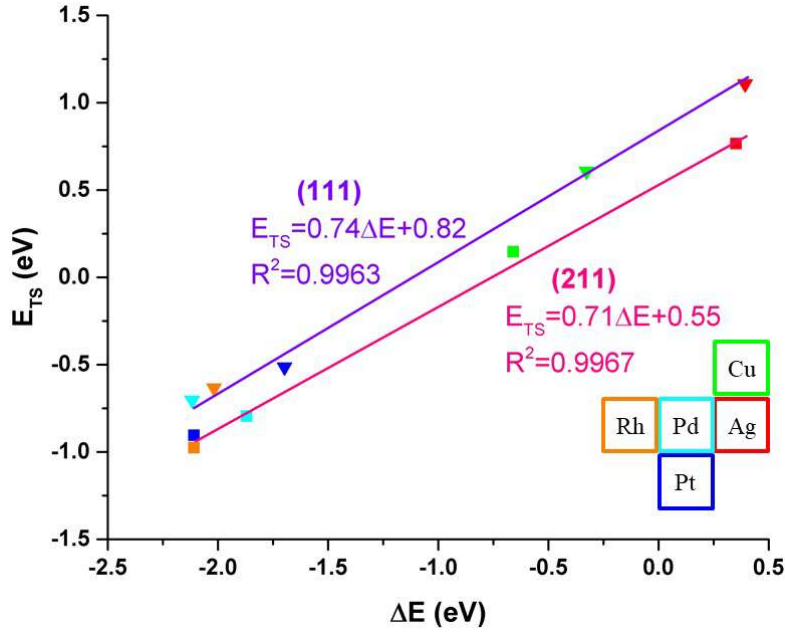


Fig. 1 Linear scaling relations between the initial and transition states of CO* hydrogenation to HCO* for the (111) and (211) facets of transition metals, represented by triangles and squares, respectively. The colors of the symbols indicate the identity of the metal according to the legend in the bottom right corner. The scaling lines for the (111) and (211) facets are in violet and pink, respectively

Plugging in the linear scaling relation into the activation energy expressions, we get:

$$\Delta E \ll 0 \quad , \quad E_a = -(1 - \alpha)\Delta E + \beta \quad | \quad \Delta E \gg 0 \quad , \quad E_a = \alpha\Delta E + \beta$$

Notice that the limiting conditions are equally valid when expressed in terms of ZPE-corrected energies instead of free energies. Therefore, when ΔE approaches either limit, the activation energy is linearly related to the initial state, with opposite slopes for these lines at the opposite limits. These lines, if extrapolated to finite ΔE , intersect precisely at $\Delta E = 0$ and at $E_a = \beta$, as shown in Fig. 2.

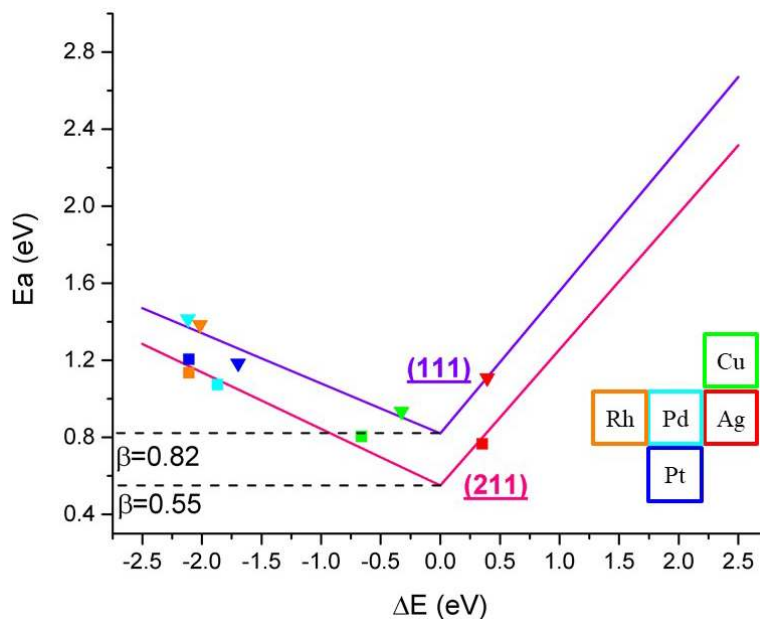


Fig. 2 The activation energy versus the initial state energy for CO* hydrogenation to HCO* on the (111) and (211) facets of transition metals, represented by triangles and squares, respectively. The colors of the symbols indicate the identity of the metal according to the legend in the bottom right corner. The scaling lines for the (111) and (211) facets are in violet and pink, respectively

To express this figure in terms of free energy, we need to add the entropy term $-TS$ to E_a (see Table S2-S4 for details). At $T = 0\text{ K}$, $E \equiv G$. We further express the free energy in terms of $-G_a$, which represents a logarithmic expression of the rate ($-G_a \sim kT \ln(r)$). This gives a volcano-like plot between the activation free energy and the ZPE-corrected energy of the initial state, with the tip of the volcano precisely at $\Delta E = 0$, as is shown in Fig. 3. This familiar volcano-type relation is a direct manifestation of the Sabatier principle, in which optimal catalysts (i.e. with the least negative $-G_a$) should not bind reaction intermediates too strongly ($\Delta E \ll 0$) or too weakly ($\Delta E \gg 0$).

The entropy term at non-zero absolute temperatures needs only be added to the $\Delta E \gg 0$ leg of the volcano, since it will largely be canceled out for ($\Delta E \ll 0$). Therefore, the $\Delta E \gg 0$ leg of the volcano is shifted downward by TS , as is shown for different temperatures in Fig. S1. To fully represent the exponent of the Arrhenius expression, we cast these volcano plots in terms of $-G_a/kT$, as is shown in Fig. 4.

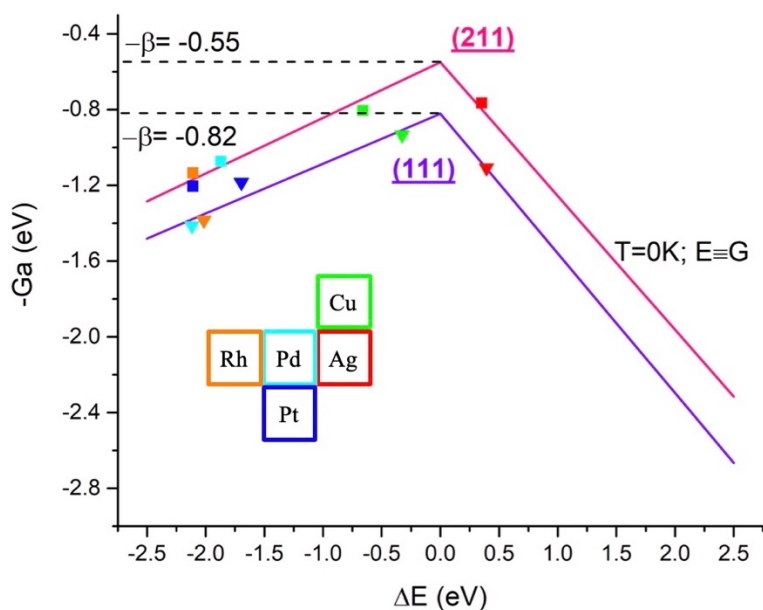


Fig. 3 The inverse of activation free energy versus the initial state energy for CO* hydrogenation to HCO* on the (111) and (211) facets of transition metals, represented by triangles and squares, respectively. The colors of the symbols indicate the identity of the metal according to the legend in the bottom left corner. The scaling lines for the (111) and (211) facets are in violet and pink, respectively

Notwithstanding the confinement of our analysis to a single elementary step in the pathway to methanol, ignoring possible side products (e.g. notably methane, which we include in the microkinetic model below), we still can make the following three predictions which follow from Fig. 4:

1. At relevant temperatures for CO hydrogenation to methanol (e.g. 500 Kelvin), Pd, Pt, and Rh appear to be more active than Cu (this will not be the case when methanation is considered through microkinetic modeling, see below).
2. The optimal catalyst should bind the initial state stronger than Cu, but weaker than Pt or Pd.
3. The optimality is temperature-dependent, given that the tip of the volcano shifts to stronger binding as the temperature increases.

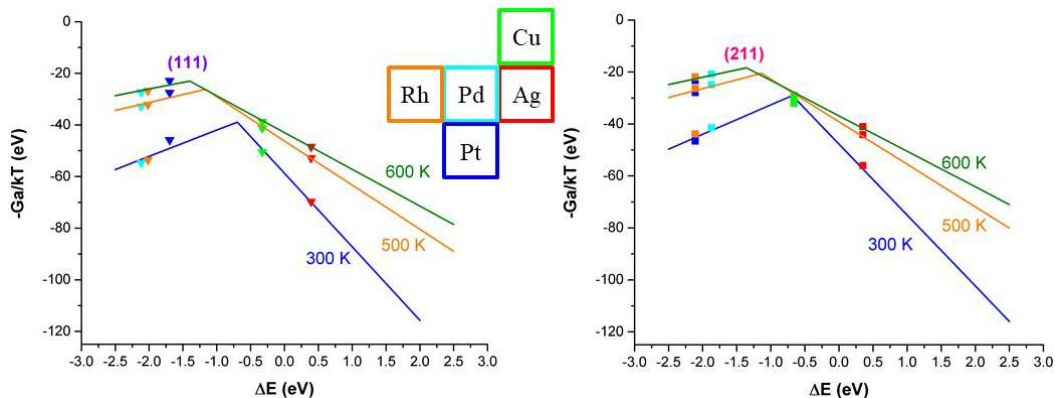


Fig. 4 $-Ga/kT$ versus the initial state energy for CO^* hydrogenation to HCO^* on the (111) and (211) facets of transition metals, represented by triangles and squares on the left and right panels, respectively. The colors of the symbols indicate the identity of the metal according to the shared legend in the middle. The symbols shift with the respective temperature lines, which are in blue, orange, and green for 300, 500, and 600 K, respectively

We now take a more general approach and analyze the full kinetic model of CO hydrogenation to methanol on the (111) surfaces. The microkinetic model [52] does not make any prior assumptions regarding the nature of the rate-determining elementary step(s). Furthermore, it considers pathways for forming methane and C_2 -oxygenates, thus providing a comprehensive scrutiny of competing side products. As descriptors, we choose the formation energies of CO^* (ΔE_{CO^*}) and the transition state (ΔE_{H-CO^*}), with the latter replacing ΔE_{OH^*} as the corresponding descriptor in our previous work[52]. This choice enables us to superimpose the linear scaling relation between these two quantities (see Fig. 1) atop the two-dimensional volcano plots produced by the microkinetic model. This, however, comes at the expense of accuracy given that the reaction intermediates which bind through their oxygen atoms do not scale as well with ΔE_{H-CO^*} as they do with ΔE_{OH^*} , e.g. OH^* and CH_3O^* (see all (111) scaling relations in Fig. S2). This is fundamentally attributed to the fact that the hybridization between the metal d states and the adsorbate states are significantly different between those adsorbates binding to the surface through carbon and those binding through oxygen, thus voiding the bond conservation arguments that makes the realization of scaling relations possible [70].

To overcome this issue, we eliminate the linear dependence of OH* and CH₃O* on the descriptors, by first setting ΔE_{OH^*} to an arbitrary constant value, and then determining the value of $\Delta E_{\text{CH}_3\text{O}^*}$ according to the scaling relation between ΔE_{OH^*} and $\Delta E_{\text{CH}_3\text{O}^*}$ (see Fig. S3). This is akin to taking a cross-section of a constant value of ΔE_{OH^*} in a three-dimensional volcano in which ΔE_{OH^*} is the third descriptor (or the third dimension). We take three such cross-sections at ΔE_{OH^*} values of 0.50, 0.00, and -0.25 eV, representing weak, moderate, and strong binding of OH*, respectively. Fig. S4-S6 show the volcano plots of the production rates of all products at these three cross sections. The main products according to the microkinetic model are methane, water, and methanol; C₂ species are produced only in trace amounts, consistent with our previous work [52]. The selectivity towards methanol versus methane is sensitive to OH* binding: at weak binding, the catalysis is more selective to methanol, while the opposite is true at moderate and strong binding. This is intelligible, given that weak binding of OH* (or interchangeably, weak binding of CH₃O*) eases methanol desorption, thus steering the catalysis towards higher selectivity to methanol. On the other hand, stronger binding of OH* (or CH₃O*) favors C-O bond splitting, and inhibits methanol desorption, shifting the selectivity towards methane. The solutions in all three cases are qualitatively similar nevertheless, and additionally, Fig. S7 shows that the solution when both ΔE_{OH^*} and $\Delta E_{\text{CH}_3\text{O}^*}$ are allowed to scale with the two descriptors is qualitatively invariant to the three cases of Fig. S4-S6.

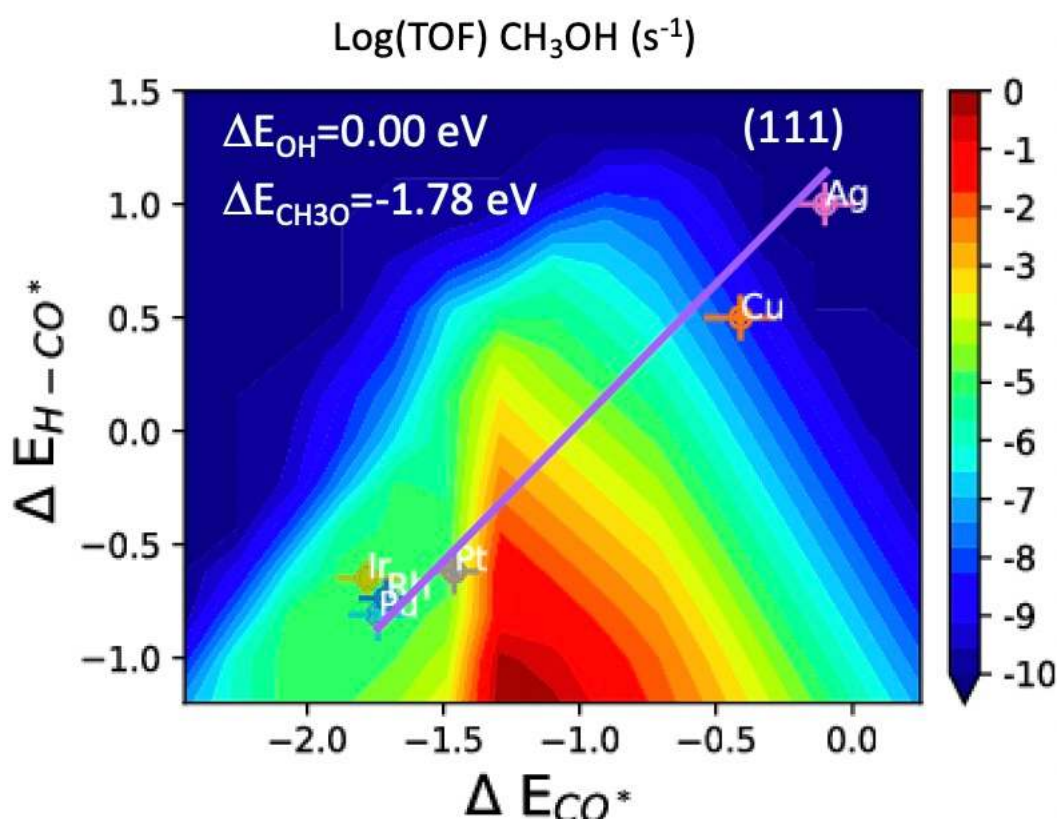


Fig. 5 Volcano plot for the rate (turnover frequency, or TOF, in s^{-1}) of methanol production via CO hydrogenation on the (111) facets of transition metals. Ir(111) was used as an extra data point for the production of this volcano plot to aid the convergence of the adsorbate-adsorbate interaction model included in the microkinetic modeling of the (111) surfaces. The TOF is plotted against the formation energies of CO^* and the transition state $H-CO^*$, allowing the superposition of the (111) linear scaling relation of Fig. 1. The error bars indicate the standard deviation of the BEEF ensemble calculations. The formation energies are relative to $CO(g)$, $H_2(g)$, and $H_2O(g)$. Improved catalysis entails the stabilization of the transition state $H-CO^*$, without further stabilizing CO^*

We now seek to analyze the volcano plot for methanol production on (111) surfaces at moderate binding of OH^* ($\Delta E_{OH} = 0.00$ eV) in greater detail (see Fig. 5). A clear peak for this activity volcano exists at moderate binding of CO^* , and significantly stabilized $H-CO^*$. The strong dependence of this peak on the transition state energy justifies the above analysis (Fig. 1-4; Fig. S1; Table S2-S4) by showing the sensitivity of the overall rate to this particular parameter. The scaling line for the (111) facets delineates an active region that lies below the line (within moderate ΔE_{CO}) and a less active region above it, which shows the central role the initial hydrogenation of CO^* to HCO^* plays in the methanol synthesis chemistry.

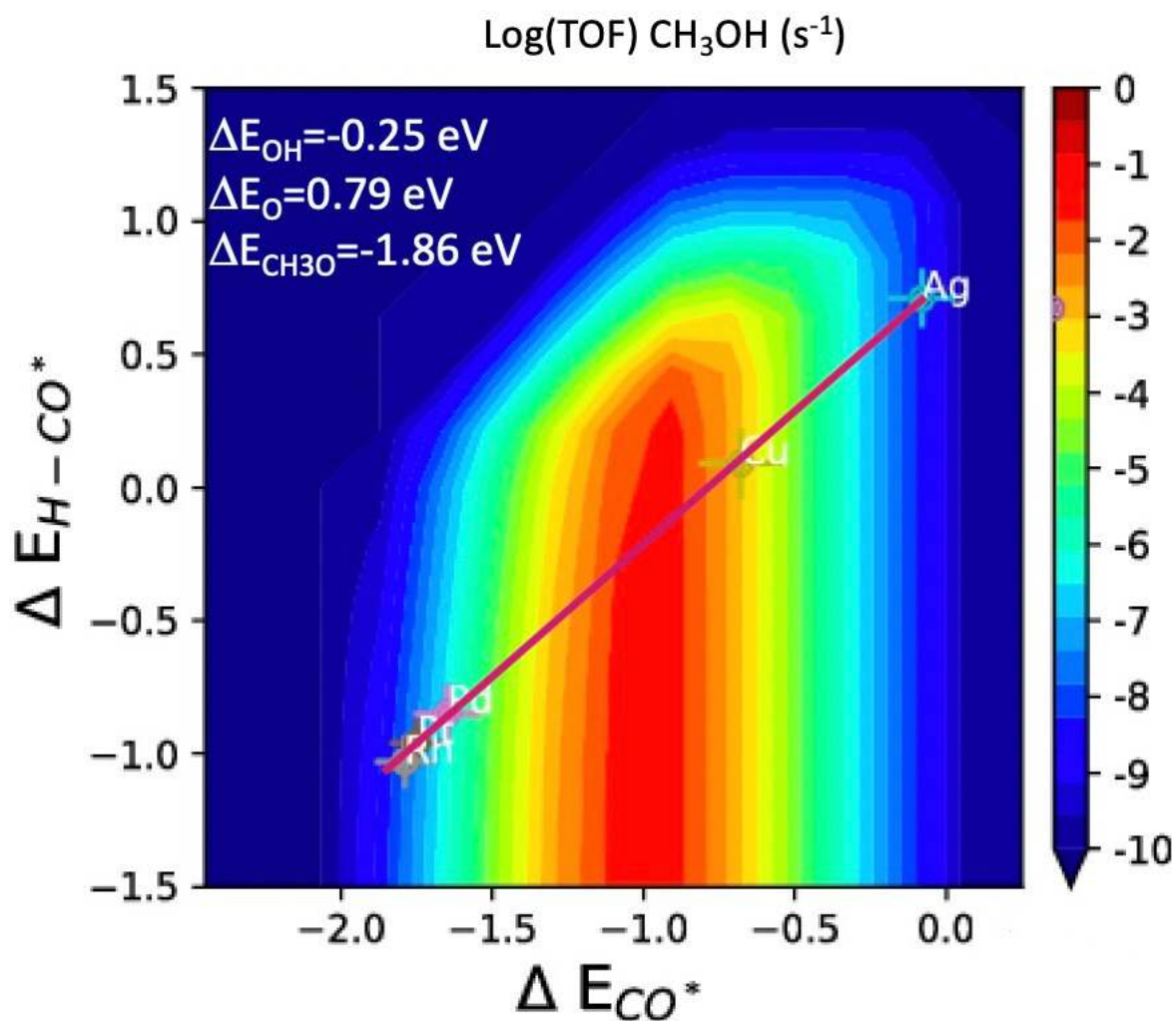


Fig. 6 Volcano plot for the rate (turnover frequency, or TOF, in s^{-1}) of methanol production via CO hydrogenation on the (211) facets of transition metals. The TOF is plotted against the formation energies of CO^* and the transition state $H-CO^*$, allowing the superposition of the (211) linear scaling relation of Fig. 1. The error bars indicate the standard deviation of the BEEF ensemble calculations. The formation energies are relative to $CO(g)$, $H_2(g)$, and $H_2O(g)$. Improved catalysis entails the destabilization of CO^* , without further destabilizing the transition state $H-CO^*$

We use the (211) data (Table S1) to construct a similar volcano plot for a reaction network that includes pathways for methane and methanol formation (we exclude C_2 species given that the (211) surfaces are known to be less selective towards higher alcohols and oxygenates [71], and given that C_2 species were hardly produced on the (111) facets anyhow). Fig. 6 shows this volcano plot at a value of $\Delta E_{OH} = -0.25$ eV, chosen to be close to ΔE_{OH} on Cu(211). Similar to the (111) volcano plots, oxygenated species do not scale well with either descriptor (see Fig. S8), and therefore, ΔE_{CH_3O} is

fixed via the scaling relation between the energies of OH and CH₃O. In addition, we also fix ΔE_{O} , thus making use of the correlation between the energies of O and OH on the (211) surfaces (on the (111) surfaces, this correlation is poor; see all O-OH-CH₃O scaling relations in Fig. S3). Like the (111) surfaces, the volcano plots are qualitatively invariant at different values of ΔE_{OH} (Fig. S9-S11) and also for the case where all oxygenated species are allowed to scale with the descriptors (Fig. S12). We see a clear dependence of the rate of methanol synthesis on $\Delta E_{\text{H-CO}^*}$ at the weak spectrum of this descriptor. However, below the scaling line at more stabilized $\Delta E_{\text{H-CO}^*}$, there seems to be little dependence of the methanol synthesis rate on $\Delta E_{\text{H-CO}^*}$. Unlike the (111) volcano plot, the (211) volcano plot does not offer a strong incentive to stabilize $\Delta E_{\text{H-CO}^*}$ independently of ΔE_{CO^*} . There is, however, a clear benefit if new catalysts that offer similar stability of the transition state to those on the strongly-adsorbing metals (Pt, Pd, and Rh), but significantly weaker binding of CO*, are found. Such new catalysts would offer significantly improved selectivity towards methanol at the expense of methane, as compared to the (211) facets of Pt, Pd, and Rh. Nonetheless, per the volcano plot of Fig. 6, those new catalysts will not be significantly more active than Cu(211) towards methanol synthesis.

We, therefore, investigate other transition states to serve as descriptors for the (211) surfaces. The goal is to discover whether there is a transition state that more significantly affects the rate towards methanol synthesis on the (211) surfaces than H-CO*. We recall that the final hydrogenation step to release methanol through hydrogenation of methoxy (CH₃O) could also be rate-determining on Cu(211), along with the initial hydrogenation step of CO* to HCO* [39]. We therefore produce the (211) volcano plots with $\Delta E_{\text{CH}_3\text{O-H}^*}$ as an activity descriptor replacing $\Delta E_{\text{H-CO}^*}$, again at $\Delta E_{\text{OH}} = -0.25$ eV (and ΔE_{O} and $\Delta E_{\text{CH}_3\text{O}}$ fixed accordingly). Fig. 7 shows this volcano plot, while Fig. S13-S14 show the corresponding (211) volcano plots employing $\Delta E_{\text{H-HCO}^*}$ and $\Delta E_{\text{H-CH}_2\text{O}^*}$ as descriptors, respectively. Notice that, like the formation energy of H-CO*, the formation energies of the other

transition states scale linearly with CO^* , though significant scatter exists for the cases of H-HCO^* and $\text{H-CH}_2\text{O}^*$ (see correlation parameters in Fig. S13-S14 captions). These volcano plots are qualitatively similar, but because of scaling with different descriptors, the values of the calculated rates at any given descriptor value-pair would be different among the different descriptors (e.g. notice the difference in rates of $\text{Cu}(211)$ predicted in Fig. 6 and Fig. 7). Fig. 7 and Fig. S13-S14 show that there are broad regions of higher activity below the scaling lines, suggesting that the transition states H-HCO^* , $\text{H-CH}_2\text{O}^*$, and $\text{CH}_3\text{O-H}^*$ could be potential targets for CO^* -independent stabilization in high-throughput screening of improved methanol synthesis catalysts. Finally, we note that all these transition states scale with one another, given their strong correlation with the formation energy of CO^* . While the goal is to escape these scaling relations as defined on transition metals, it is safe to assume that new materials would also follow their own scaling relations that are distinct from those on transition metals we identify here. This means that stabilizing any of these transition states likely entail the stabilization of the remaining ones, allowing them to be used interchangeably as screening criteria for new catalysts. Therefore, even if normally tools like degree of rate and selectivity control [72-74] could be used to determine which transition state is more rate-determining, the decision regarding which descriptor to use would likely be more dependent on the suitability of a given transition state to easy calculation and screening.

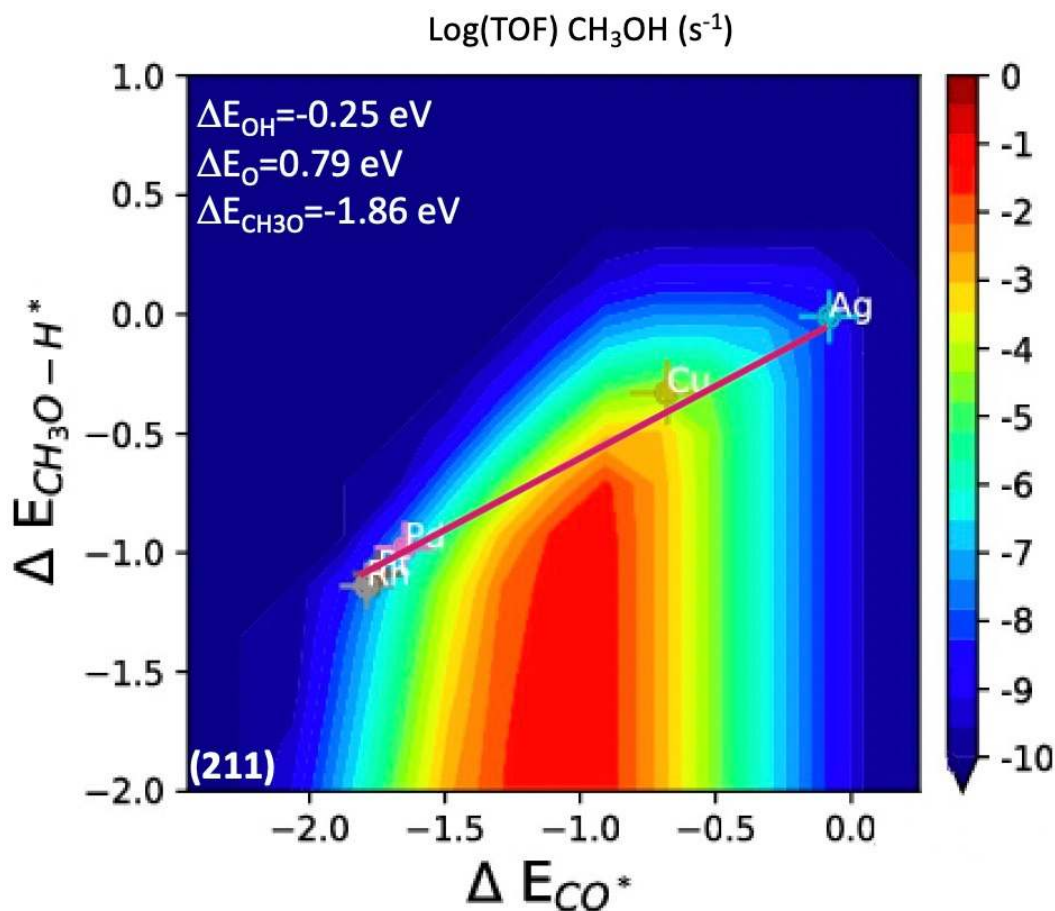


Fig. 7. Volcano plot for the rate (turnover frequency, or TOF, in s⁻¹) of methanol production via CO hydrogenation on the (211) facets of transition metals. The TOF is plotted against the formation energies of CO* and the transition state CH₃O-H*, allowing the superposition of the (211) linear scaling relation ($\Delta E_{CH_3O-H^*} = 0.66\Delta E_{CO^*} + 0.07 \text{ eV}$, $R^2=0.9949$). The error bars indicate the standard deviation of the BEEF ensemble calculations. The formation energies are relative to CO(g), H₂(g), and H₂O(g). Improved catalysis entails the stabilization of the transition state CH₃O-H*, without further stabilizing CO*

We would like to finish our discussion of the volcano plots with a few remarks regarding the positions of our surfaces on these energy maps. Ag appears to be the least active metal in CO hydrogenation due to its weak-binding characteristics, consistent with literature [75,76]. Fig. 6-7 and Fig-S13-S14 show Cu(211) to fare significantly better than Cu(111) does on Fig. 5, which is consistent with the well-established structure sensitivity of methanol synthesis on Cu surfaces [16,30-32,26,63]. Pd is well known to form a hydride phase under hydrogenation conditions [77,78], and Pd-based nanoparticles have been suggested as hydrogen storage materials due to their affinity to retaining subsurface hydrogen [79-81]. A (partial) hydride phase of Pd would lie at more active

regions of CO hydrogenation than metallic Pd does on Fig. 5. We calculated the values of the descriptors on a (2 x 2) unit cell of a PdH(111) slab model (larger unit cells affected the binding energies of CO* and H* by less than 0.10 eV). The bulk phase was taken from The Materials Project database [82], as material ID mp-24289. The formation energy of CO* on PdH(111) was calculated to be -1.33 eV; that is, 0.32 eV higher (i.e. less stable) than that on Pd(111), as detailed in Table S1. At a CO* formation energy of -1.33 eV, the scaling relation would give a formation energy value of H-CO* at -0.55 eV on PdH(111), which is close to the DFT-calculated value of -0.40 eV. Pt, Pd, and Rh were shown to have high methanol synthesis activity per the analysis of Fig. 4. Absent from Fig. 4 was any treatment of methanation, however. When a competing pathway towards methane is introduced through the microkinetic models we discussed, we predict that either facet of the strongly-adsorbing metals of Pt, Pd, and Rh will be more selective towards methane than methanol (see Fig. S15-17). Indeed, numerous reports in literature discuss the activity and selectivity of Pd, and to less extent, Pt and Rh towards methanol synthesis versus methanation [83-95], although selectivity towards methanol (vis-à-vis the competitive methane) vary widely depending on the support, presence of additives, as well as the catalyst synthesis conditions. In general, a high selectivity to methanol is attributed to the inability of these metals to dissociate the C-O bond, a prerequisite for methane formation.

4 Discussion

Fig. 5-7, S13-S14 show that there is room for development for CO hydrogenation catalysts, but this development is limited by the presence of linear scaling relations. Put another way, the challenge in methanol synthesis from syngas lies in stabilizing H-CO* and/or other transition states along the methanol synthesis pathway independent of CO*, as well as destabilizing CO* independently of the transition state energies on strongly adsorbing surfaces, thus breaking the strong linear scaling relations between the energies of these states. Interestingly, this is also a challenge for the

electrochemical reduction of CO, for which a very similar volcano plot was recently derived [96]. This materials challenge necessitates finding new catalytic materials that do not follow the scaling relations of transition metals. This is a necessary, but insufficient, condition [43] to improve the activity and selectivity towards methanol, since the selectivity would depend on the overall production rate of the several possible products based on coupled atomic-scale factors (e.g. support effects, surface reconstruction under realistic reaction conditions).

We briefly survey the literature for inspiration on how to surmount this challenge in CO hydrogenation to methanol catalysis. Typically, breaking linear scaling relations requires the realization of active sites that are geometrically and/or electronically different from those for which the linear scaling relations under question are derived [97]. Transition metal phosphides [98] and oxides [99] have demonstrated their abilities to break linear scaling relations derived on transition metals by offering significantly different active sites for adsorption of reaction intermediates. An immediate logical step to achieve this variation in geometrical/electronic properties within the class of transition metals is offered by bimetallic catalysts. The improved activity could be attributed either to the Interpolation Principle [100], in which the adsorption properties of an alloy lie in between those of its constituent metal components, or attributed to synergistic effects between the alloy constituents, pushing the performance of the alloy beyond the simple linear interpolation of those of its individual components. Bimetallic alloys have been shown to help escape the linear scaling relations governing CO* and HCO*, given that the latter interacts with the surface through either the carbon or oxygen atom, unlike CO* which only adsorbs through carbon. This might also be true of the H-CO*, if the transition state does not completely resemble the dehydrogenated state; e.g. if CO* gets tilted enough at the transition state to allow the oxygen end to interact with the surface. If one of the two components of the bimetallic alloy binds oxygen significantly differently than the other component binds carbon, then we may arrive at a bifunctional catalyst that potentially escapes the linear scaling

relations on monometallic catalysts. This bifunctionality was suggested to preferentially stabilize HCO^* compared to CO^* over the stepped surfaces of several bimetallic alloys for the electrochemical reduction of CO/CO_2 [101]. A drawback was the low stability for most of the suggested alloys, especially in the aqueous environment typical of electrochemistry. In this regard, it is worth mentioning that high entropy (quinary) alloys have been recently proposed as potentially stable and active for the electrochemical CO_2/CO reduction [102].

A special case of bimetallic alloys that have proven to be quite useful in escaping scaling relations is single atom alloys (SAAs). In SAAs, a solute metal exists in very dilute concentrations in the top layer or the immediate sublayer of the host metal. A Pt or a Pd atom embedded in other transition metals were suggested to stabilize the transition state of hydrogen dissociation without affecting the adsorption energy of atomic hydrogen [103], among several other examples for industrially-relevant chemistries [104-107]. While the massively combinatorial search space for bimetallic alloys (including bulk alloys, core@shell alloys, and SAAs) offers a great potential to arriving at surfaces that stabilize H-CO^* independently of CO^* , and despite exciting advances in the inorganic synthesis community aiming at depositing metal layers atop nanoparticles or shape-selected nanocrystals of other metals [108-115], realizing certain alloy compositions/morphologies experimentally or preserving the structures of their unique active sites under reaction conditions (e.g. against segregation/aggregation) remains an open challenge [116-121].

5 Conclusions and Outlook

We presented a trends analysis study of CO hydrogenation to methanol on the terraces and steps of transition metals, by first investigating the rate-determining step: CO^* hydrogenation to HCO^* , then by studying a full microkinetic model. By plotting the rate of methanol synthesis versus the formation energies of CO^* and H-CO^* (or other methanol synthesis transition states) as descriptors, we show a fundamental limitation for transition metal catalysis for methanol synthesis, as imposed by linear

scaling relations between the formation energy of CO* and those of the transition states along the hydrogenation pathway to methanol. The challenge in this catalysis is to find catalytic materials that are able to escape these linear scaling relations, significantly stabilizing the transition states independently of CO*, and/or destabilizing CO* independently of the transition states.

The expansive search space of materials to be explored invites clever techniques to more efficiently achieve a thorough exploration and discovery of catalytic materials that escape the unfavorable linear scaling relation of CO* and H-CO*, while performing as few DFT calculations as possible. In recent years, machine learning has emerged as a powerful tool in exploring materials search space, with special focus on the design and discovery of catalytic materials [122-126]. Recent studies employing machine learning rely on Bayesian statistics to train algorithms on data sets (either computed or derived from materials data repositories [127]) to rapidly predict relevant properties (e.g. descriptors) from the structures of proposed materials. Indeed, several recent reports have focused on relating the catalytic behavior to electronic or structural properties like generalized or orbitalwise coordination numbers [128-130], site-specific stabilities [131-134], or *d*-band moments [135], all of which are properties that machine learning models could be trained to predict on the fly. Machine learning models including non-linear regression techniques, neural networks, and Gaussian process regression have been recently employed to describe adsorption energies of important intermediates in methane to methanol conversion [136], CO/CO₂ electro-reduction and the hydrogen evolution reaction [102,137], methanol electrooxidation [138], and oxygen evolution reaction [139]. Finally, we also note that machine learning surrogate models have been suggested to calculate transition states at a fraction of the computational cost required by explicit DFT (e.g. via the nudged elastic band method) [140-142], thus making another case for using machine learning to screen materials based on transition state energies as descriptors.

In the end, we would like to discuss a few kinetic pathways that we did not investigate in this study. Specifically, the water-gas shift reaction is quite active on Cu(211) [34], Cu(111) [143] and other surfaces studied here. On either Cu surface, the reaction mechanism was calculated to proceed through a COOH* mechanism (while HCOO* acted as a spectator), and water dissociation to H* and OH* was rate-limiting. The water-gas shift reaction is significantly faster than CO (or CO₂) hydrogenation to methanol, allowing the water-gas shift reaction to equilibrate under methanol synthesis conditions. A more complete description of the kinetics of methanol synthesis should include reaction pathways for the water-gas shift reaction, as well as CO₂ hydrogenation. Additionally, higher methanol composition in the reaction mixture – a possibility on surfaces that succeed in improving the methanol yield – could affect the overall methanol yield and selectivity. To simulate this scenario, methanol was added to the synthesis gas composition in a microkinetic model for the (211) facet of transition metals [43]. As a result, selectivity towards ethanol increased at the expense of methanol, which was attributed to higher CH₃O coverage (C-O bond scission is easier in CH₃O than in CO) and an increased rate for subsequent C-C coupling elementary steps. This observation could set an additional design constraint on the new materials we proposed. In addition to lowering the barrier for C-H bond formation, C-C bond formation and C-O bond dissociation should be simultaneously suppressed. These additional constraints – however challenging given the myriad possible pathways through which C-C coupling could take place – would ensure a robust screening and computational design approach to achieve materials that would take us a step closer to the methanol economy.

Acknowledgments

The authors acknowledge support through V-Sustain: The VILLUM Centre for the Science of Sustainable Fuels and Chemicals (#20886) from VILLUM FONDEN.

Compliance with Ethical Standards

Conflict of interest - The authors declare that they have no conflict of interest.

References

1. Solomon S, Plattner GK, Knutti R, Friedlingstein P (2009) Irreversible climate change due to carbon dioxide emissions. *Proc Natl Acad Sci U S A* 106 (6):1704-1709. doi:10.1073/pnas.0812721106
2. Hamelers HVM, Schaetzle O, Paz-Garcia JM, Biesheuvel PM, Buisman CJN (2014) Harvesting Energy from CO₂ Emissions. *Environ Sci Technol Lett* 1 (1):31-35. doi:10.1021/ez4000059
3. Bahari NA, Isahak W, Masdar MS, Yaakob Z (2019) Clean hydrogen generation and storage strategies via CO₂ utilization into chemicals and fuels: A review. *Int J Energy Res* 43 (10):5128-5150. doi:10.1002/er.4498
4. Olah GA (2005) Beyond oil and gas: The methanol economy. *Angew Chem Int Ed* 44 (18):2636-2639. doi:10.1002/anie.200462121
5. Olah GA, Goepfert A, Prakash GKS (2009) Chemical Recycling of Carbon Dioxide to Methanol and Dimethyl Ether: From Greenhouse Gas to Renewable, Environmentally Carbon Neutral Fuels and Synthetic Hydrocarbons. *J Org Chem* 74 (2):487-498. doi:10.1021/jo801260f
6. Olah GA (2013) Towards Oil Independence Through Renewable Methanol Chemistry. *Angew Chem Int Ed* 52 (1):104-107. doi:10.1002/anie.201204995
7. Liu WC, Baek J, Somorjai GA (2018) The Methanol Economy: Methane and Carbon Dioxide Conversion. *Top Catal* 61 (7-8):530-541. doi:10.1007/s11244-018-0907-4
8. Cifre PG, Badr O (2007) Renewable hydrogen utilisation for the production of methanol. *Energy Conversion and Management* 48 (2):519-527. doi:10.1016/j.enconman.2006.06.011
9. Joghee P, Malik JN, Pylypenko S, O'Hayre R (2015) A review on direct methanol fuel cells - In the perspective of energy and sustainability. *MRS Energy & Sustainability* 2. doi:10.1557/mre.2015.4
10. Tian P, Wei YX, Ye M, Liu ZM (2015) Methanol to Olefins (MTO): From Fundamentals to Commercialization. *ACS Catal* 5 (3):1922-1938. doi:10.1021/acscatal.5b00007
11. Yarulina I, Chowdhury AD, Meirer F, Weckhuysen BM, Gascon J (2018) Recent trends and fundamental insights in the methanol-to-hydrocarbons process. *Nat Catal* 1 (6):398-411. doi:10.1038/s41929-018-0078-5
12. Sheldon D (2017) Methanol Production - A Technical History A review of the last 100 years of the industrial history of methanol production and a look into the future of the industry. *Johnson Matthey Technology Review* 61 (3):172-182. doi:10.1595/205651317x695622
13. Chanchlani KG, Hudgins RR, Silveston PL (1992) METHANOL SYNTHESIS FROM H₂, CO, AND CO₂ OVER CU/ZNO CATALYSTS. *J Catal* 136 (1):59-75. doi:10.1016/0021-9517(92)90106-r
14. Waugh KC (1992) METHANOL SYNTHESIS. *Catal Today* 15 (1):51-75. doi:10.1016/0920-5861(92)80122-4
15. Spencer MS (1999) The role of zinc oxide in Cu ZnO catalysts for methanol synthesis and the water-gas shift reaction. *Top Catal* 8 (3-4):259-266. doi:10.1023/a:1019181715731
16. Kasatkin I, Kurr P, Kniep B, Trunschke A, Schlögl R (2007) Role of lattice strain and defects in copper particles on the activity of Cu/ZnO/Al₂O₃ catalysts for methanol synthesis. *Angew Chem Int Ed* 46 (38):7324-7327. doi:10.1002/anie.200702600

17. Behrens M (2009) Meso- and nano-structuring of industrial Cu/ZnO/(Al₂O₃) catalysts. *J Catal* 267 (1):24-29. doi:10.1016/j.jcat.2009.07.009
18. Topsøe NY, Topsøe H (1999) On the nature of surface structural changes in Cu ZnO methanol synthesis catalysts. *Top Catal* 8 (3-4):267-270. doi:10.1023/a:1019133832569
19. d'Alnoncourt RN, Xia X, Strunk J, Löffler E, Hinrichsen O, Muhler M (2006) The influence of strongly reducing conditions on strong metal-support interactions in Cu/ZnO catalysts used for methanol synthesis. *Phys Chem Chem Phys* 8 (13):1525-1538. doi:10.1039/b515487a
20. Grunwaldt JD, Molenbroek AM, Topsøe NY, Topsøe H, Clausen BS (2000) In situ investigations of structural changes in Cu/ZnO catalysts. *J Catal* 194 (2):452-460. doi:10.1006/jcat.2000.2930
21. Nakamura I, Nakano H, Fujitani T, Uchijima T, Nakamura J (1998) Evidence for a special formate species adsorbed on the Cu-Zn active site for methanol synthesis. *Surf Sci* 402 (1-3):92-95. doi:10.1016/s0039-6028(97)00910-2
22. Nakamura J, Choi Y, Fujitani T (2003) On the issue of the active site and the role of ZnO in Cu/ZnO methanol synthesis catalysts. *Top Catal* 22 (3-4):277-285. doi:10.1023/a:1023588322846
23. Kuld S, Thorhauge M, Falsig H, Elkjaer CF, Helveg S, Chorkendorff I, Sehested J (2016) Quantifying the promotion of Cu catalysts by ZnO for methanol synthesis. *Science* 352 (6288):969-974. doi:10.1126/science.aaf0718
24. Kuld S, Conradsen C, Moses PG, Chorkendorff I, Sehested J (2014) Quantification of Zinc Atoms in a Surface Alloy on Copper in an Industrial-Type Methanol Synthesis Catalyst. *Angew Chem Int Ed* 53 (23):5941-5945. doi:10.1002/anie.201311073
25. Kattel S, Ramirez PJ, Chen JG, Rodriguez JA, Liu P (2017) CATALYSIS Active sites for CO₂ hydrogenation to methanol on Cu/ZnO catalysts. *Science* 355 (6331):1296-+. doi:10.1126/science.aal3573
26. Behrens M, Studt F, Kasatkin I, Kühl S, Hävecker M, Abild-Pedersen F, Zander S, Girgsdies F, Kurr P, Knief B-L, Tovar M, Fischer RW, Nørskov JK, Schlögl R (2012) The Active Site of Methanol Synthesis over Cu/ZnO/Al₂O₃ Industrial Catalysts. *Science* 336 (6083):893-897. doi:10.1126/science.1219831
27. Lunkenbein T, Schumann J, Behrens M, Schlögl R, Willinger MG (2015) Formation of a ZnO Overlayer in Industrial Cu/ZnO/Al₂O₃ Catalysts Induced by Strong Metal-Support Interactions. *Angew Chem Int Ed* 54 (15):4544-4548. doi:10.1002/anie.201411581
28. Schumann J, Eichelbaum M, Lunkenbein T, Thomas N, Galvan MCA, Schlögl R, Behrens M (2015) Promoting Strong Metal Support Interaction: Doping ZnO for Enhanced Activity of Cu/ZnO:M (M = Al, Ga, Mg) Catalysts. *ACS Catal* 5 (6):3260-3270. doi:10.1021/acscatal.5b00188
29. Studt F, Behrens M, Kunkes EL, Thomas N, Zander S, Tarasov A, Schumann J, Frei E, Varley JB, Abild-Pedersen F, Nørskov JK, Schlögl R (2015) The Mechanism of CO and CO₂ Hydrogenation to Methanol over Cu-Based Catalysts. *ChemCatChem* 7 (7):1105-1111. doi:10.1002/cctc.201500123
30. Yoshihara J, Campbell CT (1996) Methanol synthesis and reverse water-gas shift kinetics over Cu(110) model catalysts: Structural sensitivity. *J Catal* 161 (2):776-782. doi:10.1006/jcat.1996.0240
31. Rasmussen PB, Holmblad PM, Askgaard T, Ovesen CV, Stoltze P, Nørskov JK, Chorkendorff I (1994) METHANOL SYNTHESIS ON CU(100) FROM A BINARY GAS-MIXTURE OF CO₂ AND H₂. *Catal Lett* 26 (3-4):373-381. doi:10.1007/bf00810611
32. Szanyi J, Goodman DW (1991) METHANOL SYNTHESIS ON A CU(100) CATALYST. *Catal Lett* 10 (5-6):383-390. doi:10.1007/bf00769173
33. Gokhale AA, Dumesic JA, Mavrikakis M (2008) On the mechanism of low-temperature water gas shift reaction on copper. *J Am Chem Soc* 130 (4):1402-1414. doi:10.1021/ja0768237

34. Studt F, Behrens M, Abild-Pedersen F (2014) Energetics of the Water-Gas-Shift Reaction on the Active Sites of the Industrially Used Cu/ZnO/Al₂O₃ Catalyst. *Catal Lett* 144 (11):1973-1977. doi:10.1007/s10562-014-1363-9
35. Burke K (2012) Perspective on density functional theory. *J Chem Phys* 136 (15). doi:10.1063/1.4704546
36. Sehested J, Larsen KE, Kustov AL, Frey AM, Johannessen T, Bligaard T, Andersson MP, Norskov JK, Christensen CH (2007) Discovery of technical methanation catalysts based on computational screening. *Top Catal* 45 (1-4):9-13. doi:10.1007/s11244-007-0232-9
37. Greeley J, Mavrikakis M (2004) Alloy catalysts designed from first principles. *Nat Mater* 3 (11):810-815. doi:10.1038/nmat1223
38. Tameh MS, Dearden AK, Huang C (2018) Accuracy of Density Functional Theory for Predicting Kinetics of Methanol Synthesis from CO and CO₂ Hydrogenation on Copper. *J Phys Chem C* 122 (31):17942-17953. doi:10.1021/acs.jpcc.8b06498
39. Studt F, Abild-Pedersen F, Wu Q, Jensen AD, Temel B, Grunwaldt J-D, Nørskov JK (2012) CO hydrogenation to methanol on Cu-Ni catalysts: Theory and experiment. *J Catal* 293:51-60. doi:10.1016/j.jcat.2012.06.004
40. Studt F, Abild-Pedersen F, Varley JB, Nørskov JK (2013) CO and CO₂ Hydrogenation to Methanol Calculated Using the BEEF-vdW Functional. *Catal Lett* 143 (1):71-73. doi:10.1007/s10562-012-0947-5
41. Studt F, Sharafutdinov I, Abild-Pedersen F, Elkjaer CF, Hummelshøj JS, Dahl S, Chorkendorff I, Nørskov JK (2014) Discovery of a Ni-Ga catalyst for carbon dioxide reduction to methanol. *Nat Chem* 6 (4):320-324. doi:10.1038/nchem.1873
42. Grabow LC, Mavrikakis M (2011) Mechanism of Methanol Synthesis on Cu through CO₂ and CO Hydrogenation. *ACS Catal* 1 (4):365-384. doi:10.1021/cs200055d
43. Medford AJ, Lausche AC, Abild-Pedersen F, Temel B, Schjødt NC, Norskov JK, Studt F (2014) Activity and Selectivity Trends in Synthesis Gas Conversion to Higher Alcohols. *Top Catal* 57 (1-4):135-142. doi:10.1007/s11244-013-0169-0
44. Frei MS, Capdevila-Cortada M, Garcia-Muelas R, Mondelli C, Lopez N, Stewart JA, Ferre DC, Perez-Ramirez J (2018) Mechanism and microkinetics of methanol synthesis via CO₂ hydrogenation on indium oxide. *J Catal* 361:313-321. doi:10.1016/j.jcat.2018.03.014
45. Maulana AL, Putra RID, Saputro AG, Agusta MK, Nugraha, Dipojono HK (2019) DFT and microkinetic investigation of methanol synthesis via CO₂ hydrogenation on Ni(111)-based surfaces. *Phys Chem Chem Phys* 21 (36):20276-20286. doi:10.1039/c9cp02970b
46. van Rensburg WJ, Petersen MA, Datt MS, van den Berg JA, van Helden P (2015) On the Kinetic Interpretation of DFT-Derived Energy Profiles: Cu-Catalyzed Methanol Synthesis. *Catal Lett* 145 (2):559-568. doi:10.1007/s10562-014-1407-1
47. Tang QL, Zou WT, Huang RK, Wang Q, Duan XX (2015) Effect of the components' interface on the synthesis of methanol over Cu/ZnO from CO₂/H₂: a microkinetic analysis based on DFT plus U calculations. *Phys Chem Chem Phys* 17 (11):7317-7333. doi:10.1039/c4cp05518g
48. Nie XW, Wang HZ, Janik MJ, Chen YG, Guo XW, Song CS (2017) Mechanistic Insight into C-C Coupling over Fe-Cu Bimetallic Catalysts in CO₂ Hydrogenation. *J Phys Chem C* 121 (24):13164-13174. doi:10.1021/acs.jpcc.7b02228
49. Neurock M (1999) First-principles analysis of the hydrogenation of carbon monoxide over palladium. *Top Catal* 9 (3-4):135-152. doi:10.1023/a:1019179009796
50. Lam E, Corral-Prez JJ, Larmier K, Noh G, Wolf P, Comas-Vives A, Urakawa A, Copret C (2019) CO₂ Hydrogenation on Cu/Al₂O₃: Role of Metal/Support Interface in Driving Activity and Selectivity of a Bifunctional Catalyst. *Angew Chem Int Ed* 58 (39):13989-13996. doi:10.1002/anie.201908060

51. Medford AJ, Vojvodic A, Hummelshoj JS, Voss J, Abild-Pedersen F, Studt F, Bligaard T, Nilsson A, Norskov JK (2015) From the Sabatier principle to a predictive theory of transition-metal heterogeneous catalysis. *J Catal* 328:36-42. doi:10.1016/j.jcat.2014.12.033
52. Schumann J, Medford AJ, Yoo JS, Zhao ZJ, Bothra P, Cao A, Studt F, Abild-Pedersen F, Norskov JK (2018) Selectivity of Synthesis Gas Conversion to C₂+ Oxygenates on fcc(111) Transition-Metal Surfaces. *ACS Catal* 8 (4):3447-+. doi:10.1021/acscatal.8b00201
53. Aresta M, Dibenedetto A (2007) Utilisation of CO₂ as a chemical feedstock: opportunities and challenges. *Dalton Transactions* (28):2975-2992. doi:10.1039/b700658f
54. Rahimpour MR, Moghtaderi B, Jahanmiri A, Rezaie N (2005) Operability of an industrial methanol synthesis reactor with mixtures of fresh and partially deactivated catalyst. *Chemical Engineering & Technology* 28 (2):226-234. doi:10.1002/ceat.200407062
55. Klier K, Chatikavanij V, Herman RG, Simmons GW (1982) CATALYTIC SYNTHESIS OF METHANOL FROM CO/H₂. 4. THE EFFECTS OF CARBON-DIOXIDE. *J Catal* 74 (2):343-360. doi:10.1016/0021-9517(82)90040-9
56. Fichtl MB, Schlereth D, Jacobsen N, Kasatkin I, Schumann J, Behrens M, Schlögl R, Hinrichsen O (2015) Kinetics of deactivation on Cu/ZnO/Al₂O₃ methanol synthesis catalysts. *Applied Catalysis A-General* 502:262-270. doi:10.1016/j.apcata.2015.06.014
57. Bukhtiyarova M, Lunkenbein T, Kahler K, Schlögl R (2017) Methanol Synthesis from Industrial CO₂ Sources: A Contribution to Chemical Energy Conversion. *Catal Lett* 147 (2):416-427. doi:10.1007/s10562-016-1960-x
58. Sahibzada M, Metcalfe IS, Chadwick D (1998) Methanol synthesis from CO/CO₂/H₂ over Cu/ZnO/Al₂O₃ at differential and finite conversions. *J Catal* 174 (2):111-118. doi:10.1006/jcat.1998.1964
59. Yang Y, Mims CA, Mei DH, Peden CHF, Campbell CT (2013) Mechanistic studies of methanol synthesis over Cu from CO/CO₂/H₂/H₂O mixtures: The source of C in methanol and the role of water. *J Catal* 298:10-17. doi:10.1016/j.jcat.2012.10.028
60. Lee JS, Lee KH, Lee SY, Kim YG (1993) A COMPARATIVE-STUDY OF METHANOL SYNTHESIS FROM CO₂/H₂ AND CO/H₂ OVER A CU/ZNO/AL₂O₃ CATALYST. *J Catal* 144 (2):414-424. doi:10.1006/jcat.1993.1342
61. Liu G, Willcox D, Garland M, Kung HH (1985) THE ROLE OF CO₂ IN METHANOL SYNTHESIS ON CU-ZN OXIDE - AN ISOTOPE LABELING STUDY. *J Catal* 96 (1):251-260. doi:10.1016/0021-9517(85)90378-1
62. Gogate MR (2019) Methanol synthesis revisited: reaction mechanisms in CO/CO₂ hydrogenation over Cu/ZnO and DFT analysis. *Petroleum Science and Technology* 37 (5):603-610. doi:10.1080/10916466.2018.1558248
63. Gunter MM, Ressler T, Bems B, Buscher C, Genger T, Hinrichsen O, Muhler M, Schlögl R (2001) Implication of the microstructure of binary Cu/ZnO catalysts for their catalytic activity in methanol synthesis. *Catal Lett* 71 (1-2):37-44. doi:10.1023/a:1016696022840
64. Giannozzi P, Baroni S, Bonini N, Calandra M, Car R, Cavazzoni C, Ceresoli D, Chiarotti GL, Cococcioni M, Dabo I, Dal Corso A, de Gironcoli S, Fabris S, Fratesi G, Gebauer R, Gerstmann U, Gougoussis C, Kokalj A, Lazzeri M, Martin-Samos L, Marzari N, Mauri F, Mazzarello R, Paolini S, Pasquarello A, Paulatto L, Sbraccia C, Scandolo S, Sclauzero G, Seitsonen AP, Smogunov A, Umari P, Wentzcovitch RM (2009) QUANTUM ESPRESSO: a modular and open-source software project for quantum simulations of materials. *Journal of Physics-Condensed Matter* 21 (39). doi:10.1088/0953-8984/21/39/395502
65. Wellendorff J, Lundgaard KT, Mogelhoff A, Petzold V, Landis DD, Norskov JK, Bligaard T, Jacobsen KW (2012) Density functionals for surface science: Exchange-correlation model

- development with Bayesian error estimation. *Phys Rev B* 85 (23).
doi:10.1103/PhysRevB.85.235149
66. Monkhorst HJ, Pack JD (1976) SPECIAL POINTS FOR BRILLOUIN-ZONE INTEGRATIONS. *Phys Rev B* 13 (12):5188-5192. doi:10.1103/PhysRevB.13.5188
67. Henkelman G, Uberuaga BP, Jonsson H (2000) A climbing image nudged elastic band method for finding saddle points and minimum energy paths. *J Chem Phys* 113 (22):9901-9904. doi:10.1063/1.1329672
68. Medford AJ, Shi C, Hoffmann MJ, Lausche AC, Fitzgibbon SR, Bligaard T, Norskov JK (2015) CatMAP: A Software Package for Descriptor-Based Microkinetic Mapping of Catalytic Trends. *Catal Lett* 145 (3):794-807. doi:10.1007/s10562-015-1495-6
69. Wang S, Petzold V, Tripkovic V, Kleis J, Howalt JG, Skulason E, Fernandez EM, Hvolbaek B, Jones G, Toftelund A, Falsig H, Bjorketun M, Studt F, Abild-Pedersen F, Rossmeisl J, Norskov JK, Bligaard T (2011) Universal transition state scaling relations for (de)hydrogenation over transition metals. *Phys Chem Chem Phys* 13 (46):20760-20765. doi:10.1039/c1cp20547a
70. Abild-Pedersen F, Greeley J, Studt F, Rossmeisl J, Munter TR, Moses PG, Skúlason E, Bligaard T, Nørskov JK (2007) Scaling properties of adsorption energies for hydrogen-containing molecules on transition-metal surfaces. *Phys Rev Lett* 99 (1). doi:10.1103/PhysRevLett.99.016105
71. Yang NY, Medford AJ, Liu XY, Studt F, Bligaard T, Bent SF, Norskov JK (2016) Intrinsic Selectivity and Structure Sensitivity of Rhodium Catalysts for C₂+ Oxygenate Production. *J Am Chem Soc* 138 (11):3705-3714. doi:10.1021/jacs.5b12087
72. Campbell CT (2001) Finding the rate-determining step in a mechanism - Comparing DeDonder relations with the "degree of rate control". *J Catal* 204 (2):520-524. doi:10.1006/jcat.2001.3396
73. Foley BL, Bhan A (2020) Degree of rate control and De Donder relations – An interpretation based on transition state theory. *J Catal* 384:231-251
74. Stegelmann C, Andreasen A (2011) Finding the key transition states and intermediates controlling net reaction rates and selectivity. Available from Nature Precedings,
75. Xiao JP, Frauenheim T (2013) Theoretical Insights into CO₂ Activation and Reduction on the Ag(111) Monolayer Supported on a ZnO(000(1)under-bar) Substrate. *J Phys Chem C* 117 (4):1804-1808. doi:10.1021/jp3115868
76. Chen BWJ, Kirvassilis D, Bai YH, Mavrikakis M (2019) Atomic and Molecular Adsorption on Ag(111). *J Phys Chem C* 123 (13):7551-7566. doi:10.1021/acs.jpcc.7b11629
77. Johansson M, Skulason E, Nielsen G, Murphy S, Nielsen RM, Chorkendorff I (2010) Hydrogen adsorption on palladium and palladium hydride at 1 bar. *Surf Sci* 604 (7-8):718-729. doi:10.1016/j.susc.2010.01.023
78. Herron JA, Tonelli S, Mavrikakis M (2012) Atomic and molecular adsorption on Pd(111). *Surf Sci* 606 (21-22):1670-1679. doi:10.1016/j.susc.2012.07.003
79. Chen BWJ, Mavrikakis M (2019) Effects of composition and morphology on the hydrogen storage properties of transition metal hydrides: Insights from PtPd nanoclusters. *Nano Energy* 63. doi:10.1016/j.nanoen.2019.103858
80. Schlappbach L, Züttel A (2001) Hydrogen-storage materials for mobile applications. *Nature* 414 (6861):353-358. doi:10.1038/35104634
81. Adams BD, Chen AC (2011) The role of palladium in a hydrogen economy. *Materials Today* 14 (6):282-289. doi:10.1016/s1369-7021(11)70143-2
82. Jain A, Ong SP, Hautier G, Chen W, Richards WD, Dacek S, Cholia S, Gunter D, Skinner D, Ceder G, Persson KA (2013) Commentary: The Materials Project: A materials genome approach to accelerating materials innovation. *APL Materials* 1 (1). doi:10.1063/1.4812323

83. Lin S, Ma JY, Ye XX, Xie DQ, Guo H (2013) CO Hydrogenation on Pd(111): Competition between Fischer-Tropsch and Oxygenate Synthesis Pathways. *J Phys Chem C* 117 (28):14667-14676. doi:10.1021/jp404509v
84. Lee D, Jung GS, Lee HC, Lee JS (2006) Methanol synthesis over Pd/SiO₂ with narrow Pd size distribution prepared by using MCM-41 as a support precursor. *Catal Today* 111 (3-4):373-378. doi:10.1016/j.cattod.2005.10.062
85. Perez-Zurita MJ, Cifarelli M, Cubeiro ML, Alvarez J, Goldwasser M, Pietri E, Garcia L, Aboukais A, Lamonier JF (2003) Palladium-based catalysts for the synthesis of alcohols. *Journal of Molecular Catalysis A-Chemical* 206 (1-2):339-351. doi:10.1016/s1381-1169(03)00412-6
86. Matsumura Y, Shen WJ (2003) Methanol decomposition and synthesis over palladium catalysts. *Top Catal* 22 (3-4):271-275. doi:10.1023/a:1023536306007
87. Poutsma ML, Elek LF, Ibarbia PA, Risch AP, Rabo JA (1978) SELECTIVE FORMATION OF METHANOL FROM SYNTHESIS GAS OVER PALLADIUM CATALYSTS. *J Catal* 52 (1):157-168. doi:10.1016/0021-9517(78)90131-8
88. Chinchin GC, Denny PJ, Jennings JR, Spencer MS, Waugh KC (1988) SYNTHESIS OF METHANOL .1. CATALYSTS AND KINETICS. *Applied Catalysis* 36 (1-2):1-65. doi:10.1016/s0166-9834(00)80103-7
89. Shen WJ, Okumura M, Matsumura Y, Haruta M (2001) The influence of the support on the activity and selectivity of Pd in CO hydrogenation. *Applied Catalysis A-General* 213 (2):225-232. doi:10.1016/s0926-860x(01)00465-3
90. Matsumura Y, Shen WJ, Ichihashi Y, Okumura M (2001) Low-temperature methanol synthesis catalyzed over ultrafine palladium particles supported on cerium oxide. *J Catal* 197 (2):267-272. doi:10.1006/jcat.2000.3094
91. Hicks RF, Bell AT (1985) KINETICS OF METHANOL AND METHANE SYNTHESIS OVER PD/SIO₂ AND PD/LA₂O₃. *J Catal* 91 (1):104-115. doi:10.1016/0021-9517(85)90293-3
92. Berlowitz PJ, Goodman DW (1987) THE ACTIVITY OF PD(110) FOR METHANOL SYNTHESIS. *J Catal* 108 (2):364-368. doi:10.1016/0021-9517(87)90185-0
93. Kim CH, Lee JS, Trimm DL (2003) The preparation and characterisation of Pd-ZnO catalysts for methanol synthesis. *Top Catal* 22 (3-4):319-324. doi:10.1023/a:1023596524663
94. Gotti A, Prins R (1996) Effect of metal oxide additives on the CO hydrogenation to methanol over Rh/SiO₂ and Pd/SiO₂. *Catal Lett* 37 (3-4):143-151. doi:10.1007/bf00807745
95. Shen WJ, Ichihashi Y, Okumura M, Matsumura Y (2000) Methanol synthesis from carbon monoxide and hydrogen catalyzed over Pd/CeO₂ prepared by the deposition-precipitation method. *Catal Lett* 64 (1):23-25. doi:10.1023/a:1019070516657
96. Ulissi ZW, Tang MT, Xiao JP, Liu XY, Torelli DA, Karamad M, Cummins K, Hahn C, Lewis NS, Jaramillo TF, Chan KR, Norskov JK (2017) Machine-Learning Methods Enable Exhaustive Searches for Active Bimetallic Facets and Reveal Active Site Motifs for CO₂ Reduction. *ACS Catal* 7 (10):6600-6608. doi:10.1021/acscatal.7b01648
97. Greeley J (2016) Theoretical Heterogeneous Catalysis: Scaling Relationships and Computational Catalyst Design. *Annu Rev Chem Biomol Eng*, Vol 7 7:605-635. doi:10.1146/annurev-chembioeng-080615-034413
98. Duyar MS, Tsai C, Snider JL, Singh JA, Gallo A, Yoo JS, Medford AJ, Abild-Pedersen F, Studt F, Kibsgaard J, Bent SF, Norskov JK, Jaramillo TF (2018) A Highly Active Molybdenum Phosphide Catalyst for Methanol Synthesis from CO and CO₂. *Angew Chem Int Ed* 57 (46):15045-15050. doi:10.1002/anie.201806583
99. Sandberg RB, Hansen MH, Norskov JK, Abild-Pedersen F, Bajdich M (2018) Strongly Modified Scaling of CO Hydrogenation in Metal Supported TiO Nanostripes. *ACS Catal* 8 (11):10555-10563. doi:10.1021/acscatal.8b03327

100. Jacobsen CJH, Dahl S, Clausen BS, Bahn S, Logadottir A, Nørskov JK (2001) Catalyst design by interpolation in the periodic table: Bimetallic ammonia synthesis catalysts. *J Am Chem Soc* 123 (34):8404-8405. doi:10.1021/ja010963d
101. Hansen HA, Shi C, Lausche AC, Peterson AA, Nørskov JK (2016) Bifunctional alloys for the electroreduction of CO₂ and CO. *Phys Chem Chem Phys* 18 (13):9194-9201. doi:10.1039/c5cp07717f
102. Pedersen JK, Batchelor TAA, Bagger A, Rossmeisl J (2020) High-Entropy Alloys as Catalysts for the CO₂ and CO Reduction Reactions. *ACS Catal* 10 (3):2169-2176. doi:10.1021/acscatal.9b04343
103. Greeley J, Mavrikakis M (2006) Near-surface alloys for hydrogen fuel cell applications. *Catal Today* 111 (1-2):52-58. doi:10.1016/j.cattod.2005.10.009
104. Darby MT, Reocreux R, Sykes ECH, Michaelides A, Stamatakis M (2018) Elucidating the Stability and Reactivity of Surface Intermediates on Single-Atom Alloy Catalysts. *ACS Catal* 8 (6):5038-5050. doi:10.1021/acscatal.8b00881
105. Darby MT, Stamatakis M, Michaelides A, Sykes ECH (2018) Lonely Atoms with Special Gifts: Breaking Linear Scaling Relationships in Heterogeneous Catalysis with Single-Atom Alloys. *J Phys Chem Lett* 9 (18):5636-5646. doi:10.1021/acs.jpcllett.8b01888
106. Marcinkowski MD, Darby MT, Liu JL, Wimple JM, Lucci FR, Lee S, Michaelides A, Flytzani-Stephanopoulos M, Stamatakis M, Sykes ECH (2018) Pt/Cu single-atom alloys as coke-resistant catalysts for efficient C-H activation. *Nat Chem* 10 (3):325-332. doi:10.1038/nchem.2915
107. Liu JL, Lucci FR, Yang M, Lee S, Marcinkowski MD, Therrien AJ, Williams CT, Sykes ECH, Flytzani-Stephanopoulos M (2016) Tackling CO Poisoning with Single-Atom Alloy Catalysts. *J Am Chem Soc* 138 (20):6396-6399. doi:10.1021/jacs.6b03339
108. Brankovic SR, Wang JX, Adžić RR (2001) Metal monolayer deposition by replacement of metal adlayers on electrode surfaces. *Surf Sci* 474 (1-3):L173-L179. doi:10.1016/s0039-6028(00)01103-1
109. Yang L, Vukmirovic MB, Su D, Sasaki K, Herron JA, Mavrikakis M, Liao S, Adzic RR (2013) Tuning the Catalytic Activity of Ru@Pt Core-Shell Nanoparticles for the Oxygen Reduction Reaction by Varying the Shell Thickness. *J Phys Chem C* 117 (4):1748-1753. doi:10.1021/jp309990e
110. Sasaki K, Naohara H, Cai Y, Choi YM, Liu P, Vukmirovic MB, Wang JX, Adzic RR (2010) Core-Protected Platinum Monolayer Shell High-Stability Electrocatalysts for Fuel-Cell Cathodes. *Angew Chem Int Ed* 49 (46):8602-8607. doi:10.1002/anie.201004287
111. Semagina N, Kiwi-Minsker L (2009) Recent Advances in the Liquid-Phase Synthesis of Metal Nanostructures with Controlled Shape and Size for Catalysis. *Catalysis Reviews-Science and Engineering* 51 (2):147-217. doi:10.1080/01614940802480379
112. Xia YN, Xia XH, Wang Y, Xie SF (2013) Shape-controlled synthesis of metal nanocrystals. *MRS Bull* 38 (4):335-344. doi:10.1557/mrs.2013.84
113. Ruditskiy A, Choi S-I, Peng H-C, Xia Y (2014) Shape-controlled metal nanocrystals for catalytic applications. *MRS Bull* 39 (8):727-737. doi:10.1557/mrs.2014.167
114. Ruditskiy A, Peng HC, Xia YN (2016) Shape-Controlled Metal Nanocrystals for Heterogeneous Catalysis. *Annu Rev Chem Biomol Eng*, Vol 7 7:327-348. doi:10.1146/annurev-chembioeng-080615-034503
115. Xia YN, Xia XH, Peng HC (2015) Shape-Controlled Synthesis of Colloidal Metal Nanocrystals: Thermodynamic versus Kinetic Products. *J Am Chem Soc* 137 (25):7947-7966. doi:10.1021/jacs.5b04641

116. Nerlov J, Chorkendorff I (1998) Promotion through gas phase induced surface segregation: methanol synthesis from CO, CO₂ and H₂ over Ni/Cu(100). *Catal Lett* 54 (4):171-176. doi:10.1023/a:1019033517855
117. Nerlov J, Chorkendorff I (1999) Methanol synthesis from CO₂, CO, and H₂ over Cu(100) and Ni/Cu(100). *J Catal* 181 (2):271-279. doi:10.1006/jcat.1998.2301
118. Nerlov J, Sckerl S, Wambach J, Chorkendorff I (2000) Methanol synthesis from CO₂, CO and H₂ over Cu(100) and Cu(100) modified by Ni and Co. *Applied Catalysis A-General* 191 (1-2):97-109. doi:10.1016/s0926-860x(99)00311-7
119. Zegkinoglou I, Pielsticker L, Han ZK, Divins NJ, Kordus D, Chen YT, Escudero C, Perez-Dieste V, Zhu BE, Gao Y, Cuenya BR (2019) Surface Segregation in CuNi Nanoparticle Catalysts During CO₂ Hydrogenation: The Role of CO in the Reactant Mixture. *J Phys Chem C* 123 (13):8421-8428. doi:10.1021/acs.jpcc.8b09912
120. Darby MT, Sykes ECH, Michaelides A, Stamatakis M (2018) Carbon Monoxide Poisoning Resistance and Structural Stability of Single Atom Alloys. *Top Catal* 61 (5-6):428-438. doi:10.1007/s11244-017-0882-1
121. Papanikolaou KG, Darby MT, Stamatakis M (2019) CO-Induced Aggregation and Segregation of Highly Dilute Alloys: A Density Functional Theory Study. *J Phys Chem C* 123 (14):9128-9138. doi:10.1021/acs.jpcc.9b00649
122. Tran K, Palizhati A, Back S, Ulissi ZW (2018) Dynamic Workflows for Routine Materials Discovery in Surface Science. *Journal of Chemical Information and Modeling* 58 (12):2392-2400. doi:10.1021/acs.jcim.8b00386
123. Ulissi ZW, Medford AJ, Bligaard T, Norskov JK (2017) To address surface reaction network complexity using scaling relations machine learning and DFT calculations. *Nat Commun* 8. doi:10.1038/ncomms14621
124. Ward L, Aykol M, Blaiszik B, Foster I, Meredig B, Saal J, Suram S (2018) Strategies for accelerating the adoption of materials informatics. *MRS Bull* 43 (9):683-689. doi:10.1557/mrs.2018.204
125. Schmidt J, Marques MRG, Botti S, Marques MAL (2019) Recent advances and applications of machine learning in solid-state materials science. *Npj Comput Mater* 5. doi:10.1038/s41524-019-0221-0
126. Lamoureux PS, Winther KT, Torres JAG, Streibel V, Zhao M, Bajdich M, Abild-Pedersen F, Bligaard T (2019) Machine Learning for Computational Heterogeneous Catalysis. *ChemCatChem* 11 (16):3579-3599. doi:10.1002/cctc.201900595
127. Lin LS (2015) Materials Databases Infrastructure Constructed by First Principles Calculations: A Review. *Materials Performance and Characterization* 4 (1):148-169. doi:10.1520/mpc20150014
128. Ma XF, Xin HL (2017) Orbitalwise Coordination Number for Predicting Adsorption Properties of Metal Nanocatalysts. *Phys Rev Lett* 118 (3). doi:10.1103/PhysRevLett.118.036101
129. Calle-Vallejo F, Martinez JI, Garcia-Lastra JM, Sautet P, Loffreda D (2014) Fast Prediction of Adsorption Properties for Platinum Nanocatalysts with Generalized Coordination Numbers. *Angew Chem Int Ed* 53 (32):8316-8319. doi:10.1002/anie.201402958
130. Calle-Vallejo F, Bandarenka AS (2018) Enabling Generalized Coordination Numbers to Describe Strain Effects. *ChemSusChem* 11 (11):1824-1828. doi:10.1002/cssc.201800569
131. Choksi TS, Roling LT, Streibel V, Abild-Pedersen F (2019) Predicting Adsorption Properties of Catalytic Descriptors on Bimetallic Nanoalloys with Site-Specific Precision. *J Phys Chem Lett* 10 (8):1852-1859. doi:10.1021/acs.jpcclett.9b00475
132. Roling LT, Li L, Abild-Pedersen F (2017) Configurational Energies of Nanoparticles Based on Metal-Metal Coordination. *J Phys Chem C* 121 (41):23002-23010. doi:10.1021/acs.jpcc.7b08438

133. Roling LT, Abild-Pedersen F (2018) Structure-Sensitive Scaling Relations: Adsorption Energies from Surface Site Stability. *ChemCatChem* 10 (7):1643-1650. doi:10.1002/cctc.201701841
134. Roling LT, Choksi TS, Abild-Pedersen F (2019) A coordination-based model for transition metal alloy nanoparticles. *Nanoscale* 11 (10):4438-4452. doi:10.1039/c9nr00959k
135. Andersen M, Levchenko SV, Scheffler M, Reuter K (2019) Beyond Scaling Relations for the Description of Catalytic Materials. *ACS Catal* 9 (4):2752-2759. doi:10.1021/acscatal.8b04478
136. Toyao T, Suzuki K, Kikuchi S, Takakusagi S, Shimizu K, Takigawa I (2018) Toward Effective Utilization of Methane: Machine Learning Prediction of Adsorption Energies on Metal Alloys. *J Phys Chem C* 122 (15):8315-8326. doi:10.1021/acs.jpcc.7b12670
137. Tran K, Ulissi ZW (2018) Active learning across intermetallics to guide discovery of electrocatalysts for CO₂ reduction and H₂ evolution. *Nat Catal* 1 (9):696-703. doi:10.1038/s41929-018-0142-1
138. Li Z, Wang SW, Chin WS, Achenie LE, Xin HL (2017) High-throughput screening of bimetallic catalysts enabled by machine learning. *Journal of Materials Chemistry A* 5 (46):24131-24138. doi:10.1039/c7ta01812f
139. Back S, Tran K, Ulissi ZW (2019) Toward a Design of Active Oxygen Evolution Catalysts: Insights from Automated Density Functional Theory Calculations and Machine Learning. *ACS Catal* 9 (9):7651-7659. doi:10.1021/acscatal.9b02416
140. Singh AR, Rohr BA, Gauthier JA, Norskov JK (2019) Predicting Chemical Reaction Barriers with a Machine Learning Model. *Catal Lett* 149 (9):2347-2354. doi:10.1007/s10562-019-02705-x
141. Peterson AA (2016) Acceleration of saddle-point searches with machine learning. *J Chem Phys* 145 (7). doi:10.1063/1.4960708
142. Torres JAG, Jennings PC, Hansen MH, Boes JR, Bligaard T (2019) Low-Scaling Algorithm for Nudged Elastic Band Calculations Using a Surrogate Machine Learning Model. *Phys Rev Lett* 122 (15). doi:10.1103/PhysRevLett.122.156001
143. Grabow LC, Mavrikakis M (2011) Mechanism of Methanol Synthesis on Cu through CO₂ and CO Hydrogenation. *ACS Catal* 1 (4):365-384. doi:10.1021/cs200055d

Supporting Information for

The Challenge of CO Hydrogenation to Methanol: Fundamental Limitations

Imposed By Linear Scaling Relations

Ahmed O. Elnabawy¹, Julia Schumann², Pallavi Bothra³, Ang Cao¹, Jens K. Nørskov^{1*}

¹Department of Physics, Technical University of Denmark, Lyngby DK-2800, Denmark

²Current address: Department of Physics and Astronomy, University College London, London, United Kingdom; Department of Chemical Engineering, University College London, London, United Kingdom

³Current address: Department of Chemical and Biomolecular Engineering, Los Angeles, CA 90024, United States

Corresponding author: Jens K. Nørskov. E-mail: jkno@dtu.dk

ORCID:

Ahmed O. Elnabawy: 0000-0002-8911-1916

Julia Schumann: 0000-0002-4041-0165

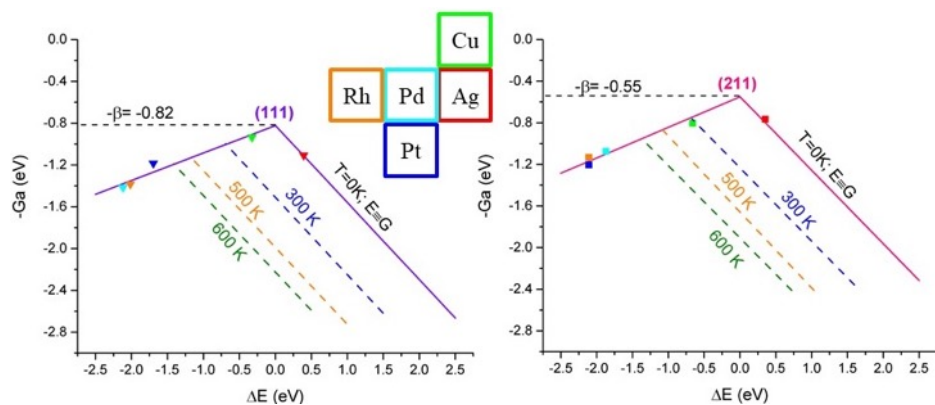


Fig. S5 The inverse of activation free energy versus the initial state energy for CO* hydrogenation to HCO* on the (111) and (211) facets of transition metals, represented by triangles and squares in the left and right panels, respectively. The colors of the symbols indicate the identity of the metal according to the legend in the bottom right corner. The scaling lines for the (111) and (211) facets are in violet and pink, respectively

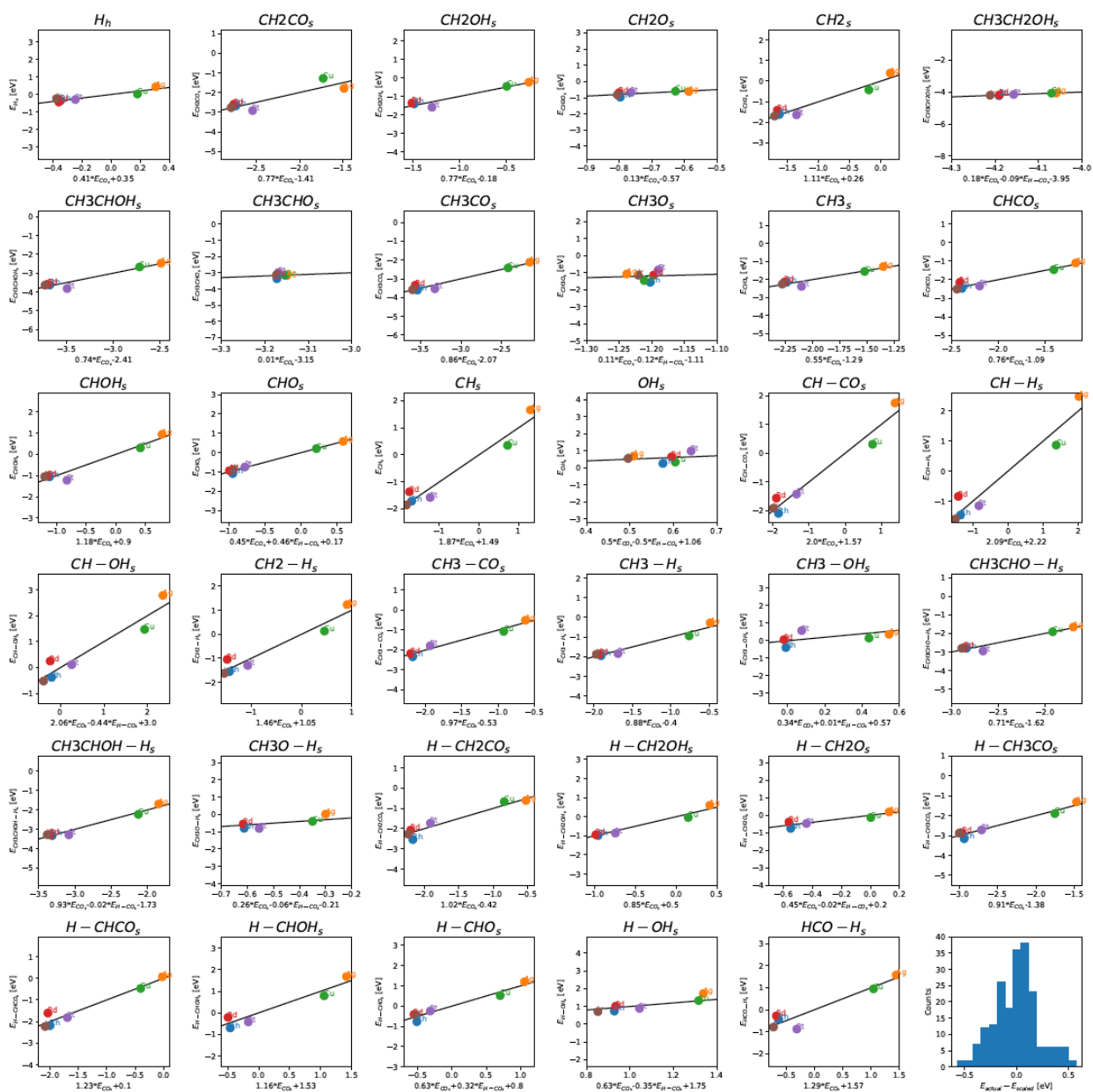


Fig. S2 Scaling relations on the (111) surfaces between the formation energies of the intermediates and transition states versus the formation energies of the descriptors CO^* and H-CO^* . The intermediates OH^* and CH_3O^* do not scale well with the descriptors

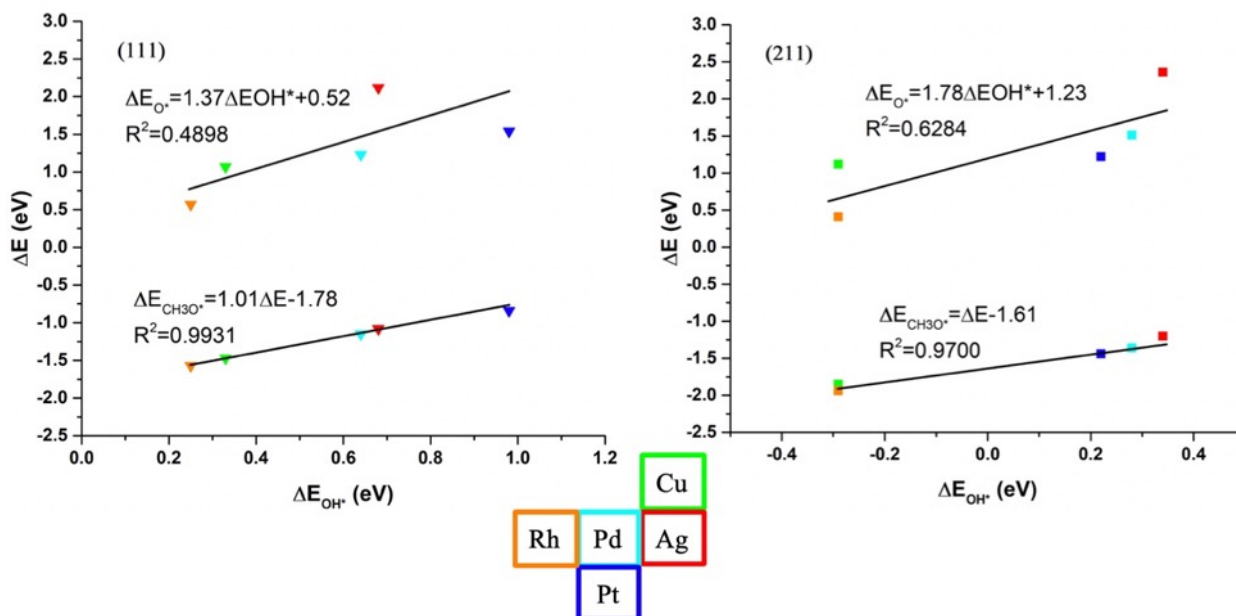


Fig. S3 Linear scaling relations between the formation energies of OH*, O*, and CH₃O* for the (111) and (211) facets of transition metals, represented by triangles (left panel) and squares (right panel), respectively. The colors of the symbols indicate the identity of the metal according to the legend in the bottom. All formation energies are relative to CO(g), H₂(g), and H₂O(g)

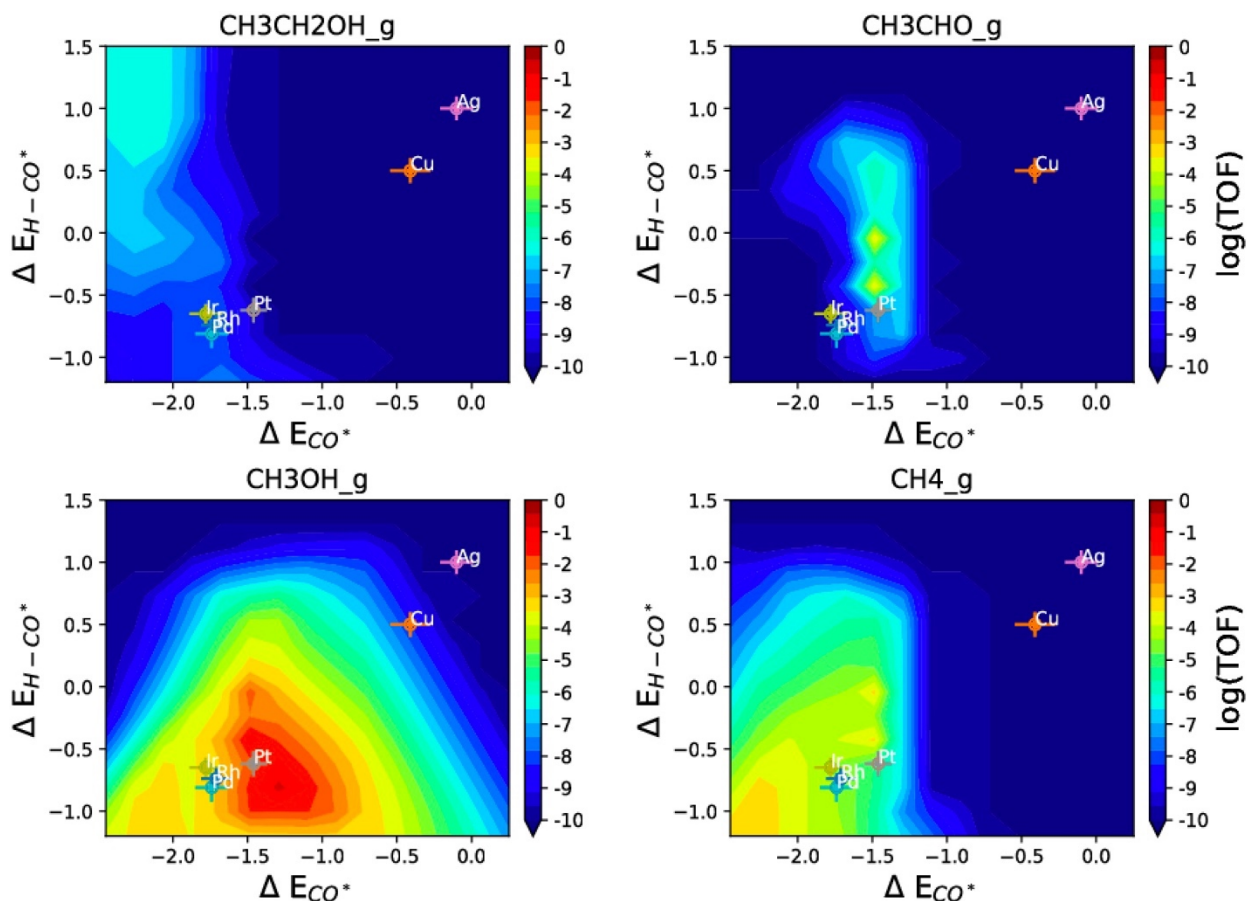


Fig. S4 Volcano plots for the rates (turnover frequency, or TOF, in s^{-1}) of ethanol, acetaldehyde, methanol, and methane on the (111) facets of transition metals, at $\Delta E_{\text{OH}} = 0.50$ eV and $\Delta E_{\text{CH}_3\text{O}} = -1.28$ eV. The TOF is plotted against the formation energies of CO^* and the transition state H-CO^* . The error bars indicate the standard deviation of the BEEF ensemble calculations. The formation energies are relative to $\text{CO}(\text{g})$, $\text{H}_2(\text{g})$ and $\text{H}_2\text{O}(\text{g})$. Methanol and methane are the majority products

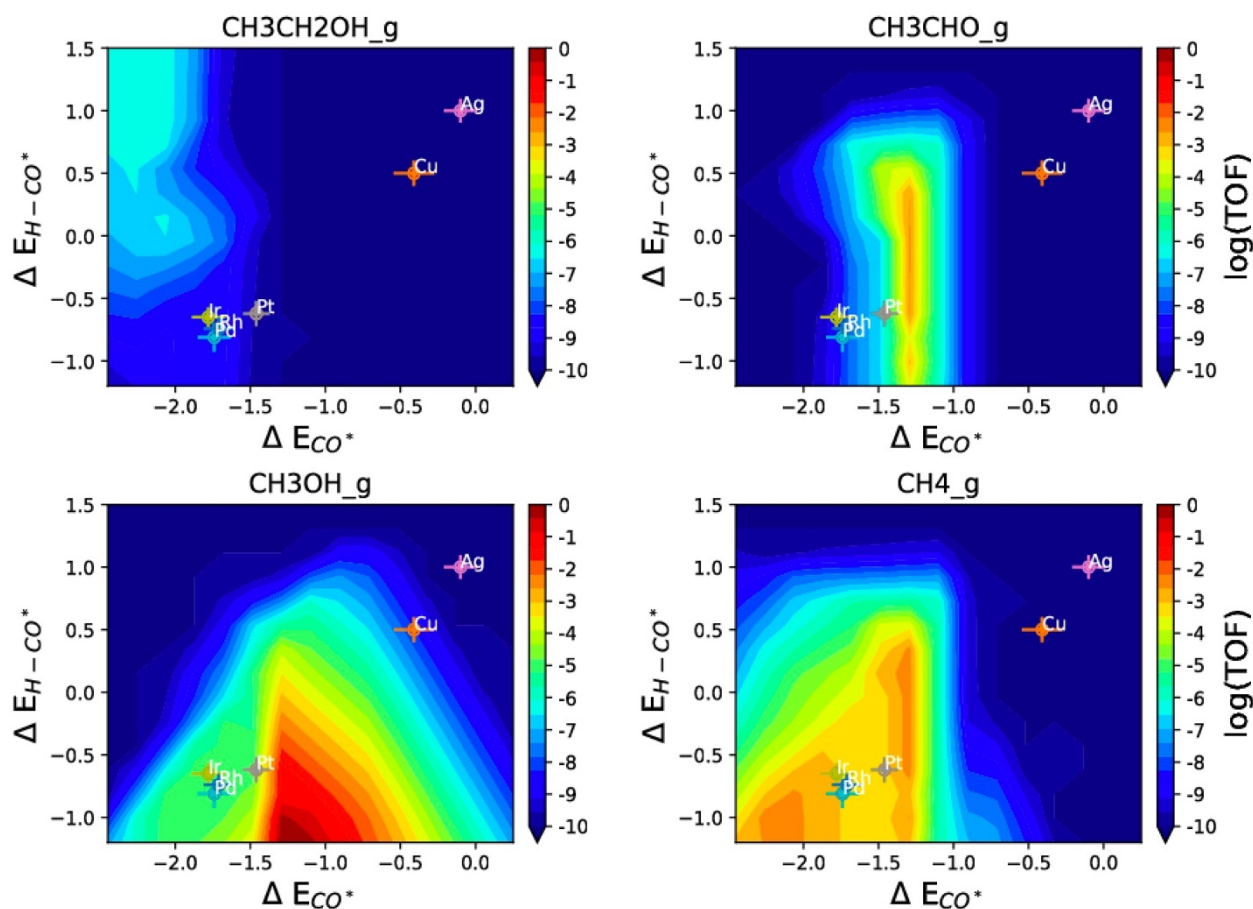


Fig. S5 Volcano plots for the rates (turnover frequency, or TOF, in s^{-1}) of ethanol, acetaldehyde, methanol, and methane on the (111) facets of transition metals, at $\Delta E_{OH} = 0.00$ eV and $\Delta E_{CH_3O} = -1.78$ eV. The TOF is plotted against the formation energies of CO^* and the transition state $H-CO^*$. The error bars indicate the standard deviation of the BEEF ensemble calculations. The formation energies are relative to $CO(g)$, $H_2(g)$ and $H_2O(g)$. Methanol and methane are the majority products

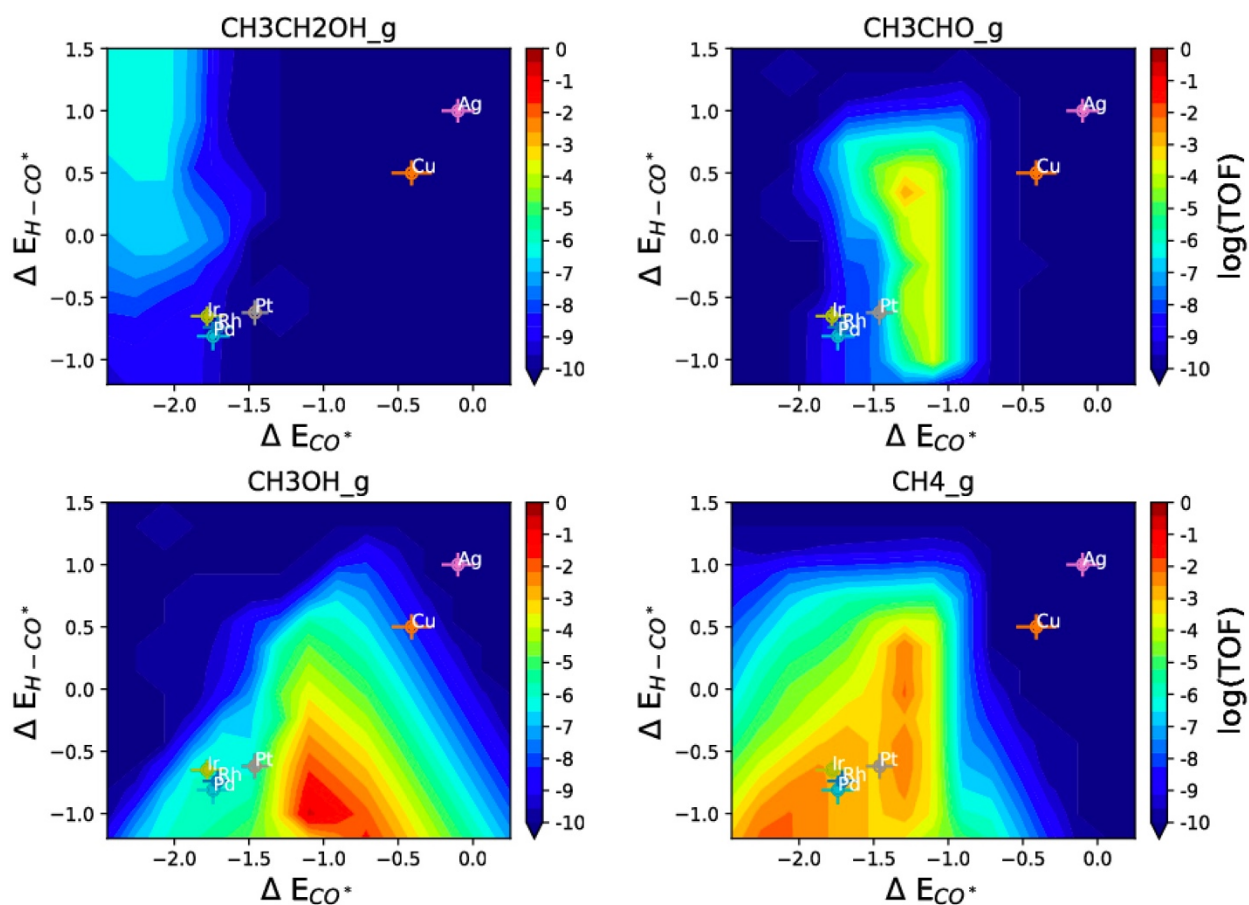


Fig. S6 Volcano plots for the rates (turnover frequency, or TOF, in s^{-1}) of ethanol, acetaldehyde, methanol, and methane on the (111) facets of transition metals, at $\Delta E_{\text{OH}} = -0.25$ eV and $\Delta E_{\text{CH}_3\text{O}} = -2.03$ eV. The TOF is plotted against the formation energies of CO^* and the transition state H-CO^* . The error bars indicate the standard deviation of the BEEF ensemble calculations. The formation energies are relative to $\text{CO}(\text{g})$, $\text{H}_2(\text{g})$ and $\text{H}_2\text{O}(\text{g})$. Methanol and methane are the majority products

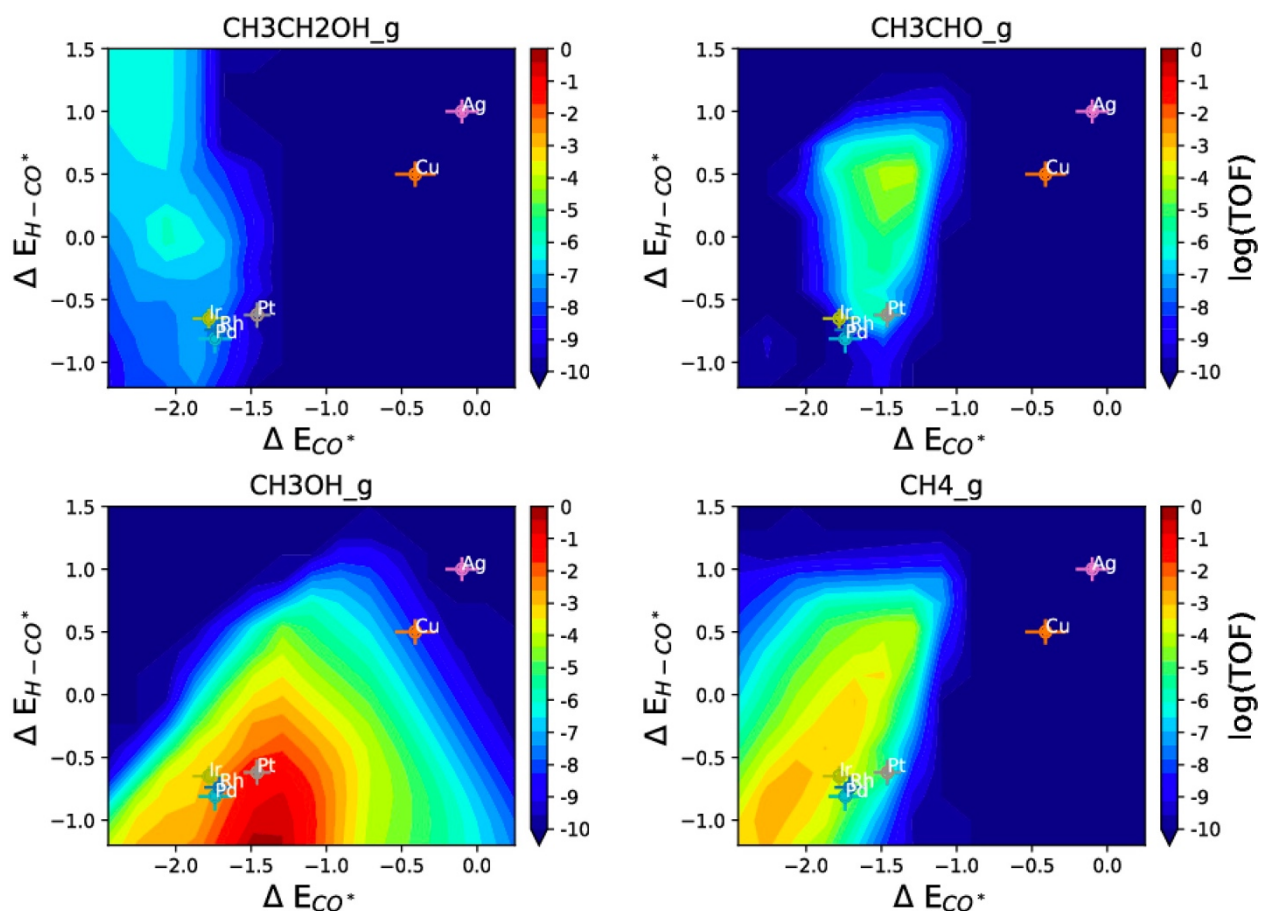


Fig. S7 Volcano plots for the rates (turnover frequency, or TOF, in s^{-1}) of ethanol, acetaldehyde, methanol, and methane on the (111) facets of transition metals. The TOF is plotted against the formation energies of CO^* and the transition state H-CO^* . The error bars indicate the standard deviation of the BEEF ensemble calculations. The formation energies are relative to $\text{CO}(\text{g})$, $\text{H}_2(\text{g})$ and $\text{H}_2\text{O}(\text{g})$. Methanol and methane are the majority products

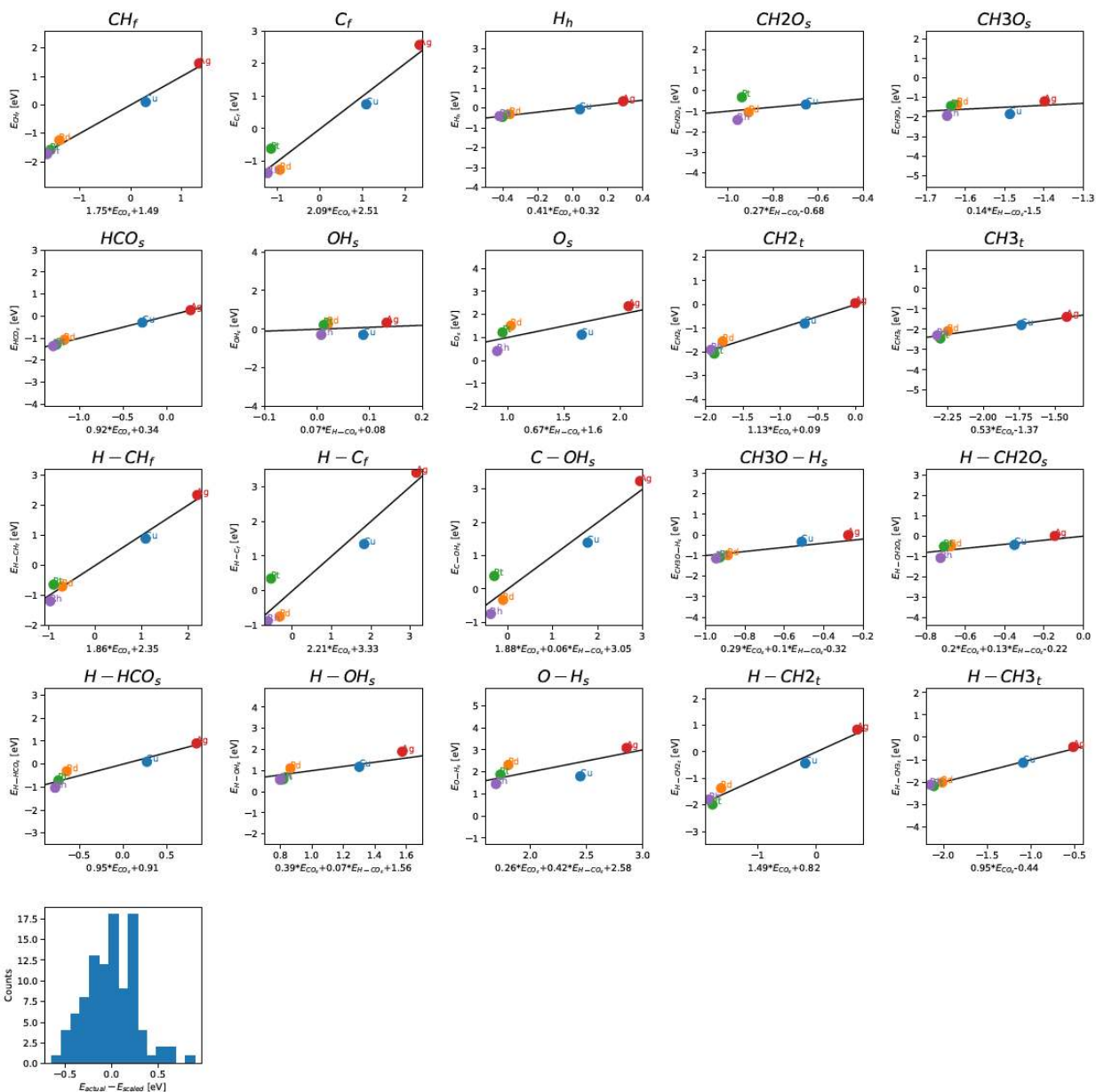


Fig. S8 Scaling relations on the (211) surfaces between the formation energies of the intermediates and transition states versus the formation energies of the descriptors CO^* and H-CO^* . The intermediates OH^* and CH_3O^* , and to less extent O^* , do not scale well with the descriptors

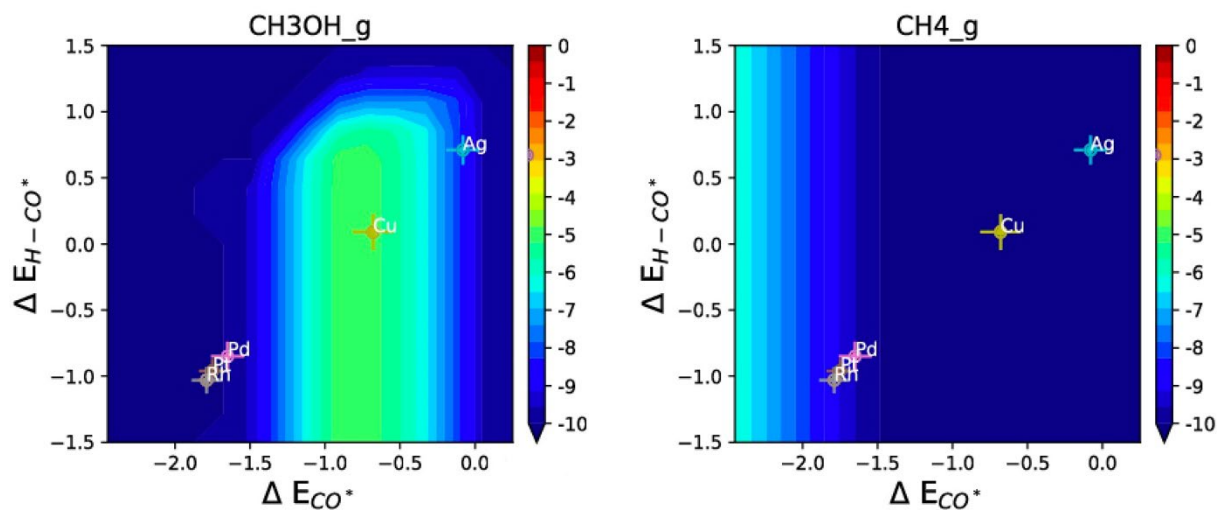


Fig. S9 Volcano plots for the rates (turnover frequency, or TOF, in s^{-1}) of methanol and methane on the (211) facets of transition metals, at $\Delta E_{\text{OH}} = 0.50$ eV, $\Delta E_{\text{O}} = 2.12$ eV, and $\Delta E_{\text{CH}_3\text{O}} = -1.11$ eV. The TOF is plotted against the formation energies of CO^* and the transition state H-CO^* . The error bars indicate the standard deviation of the BEEF ensemble calculations. The formation energies are relative to $\text{CO}(\text{g})$, $\text{H}_2(\text{g})$ and $\text{H}_2\text{O}(\text{g})$

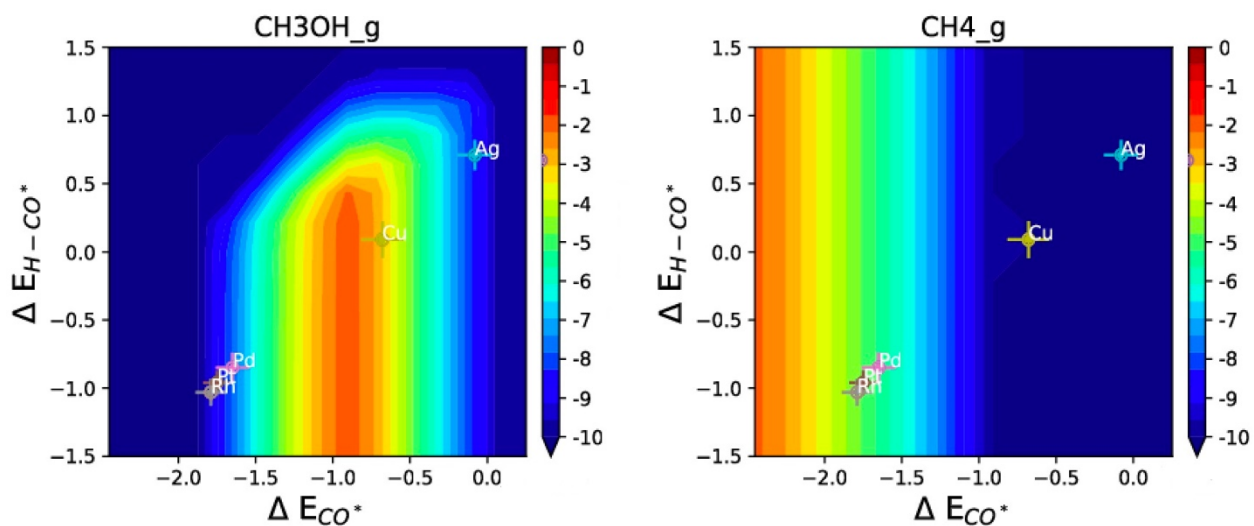


Fig. S10 Volcano plots for the rates (turnover frequency, or TOF, in s^{-1}) of methanol and methane on the (211) facets of transition metals, at $\Delta E_{OH} = 0.00$ eV, $\Delta E_O = 1.23$ eV, and $\Delta E_{CH_3O} = -1.61$ eV. The TOF is plotted against the formation energies of CO^* and the transition state $H-CO^*$. The error bars indicate the standard deviation of the BEEF ensemble calculations. The formation energies are relative to $CO(g)$, $H_2(g)$ and $H_2O(g)$

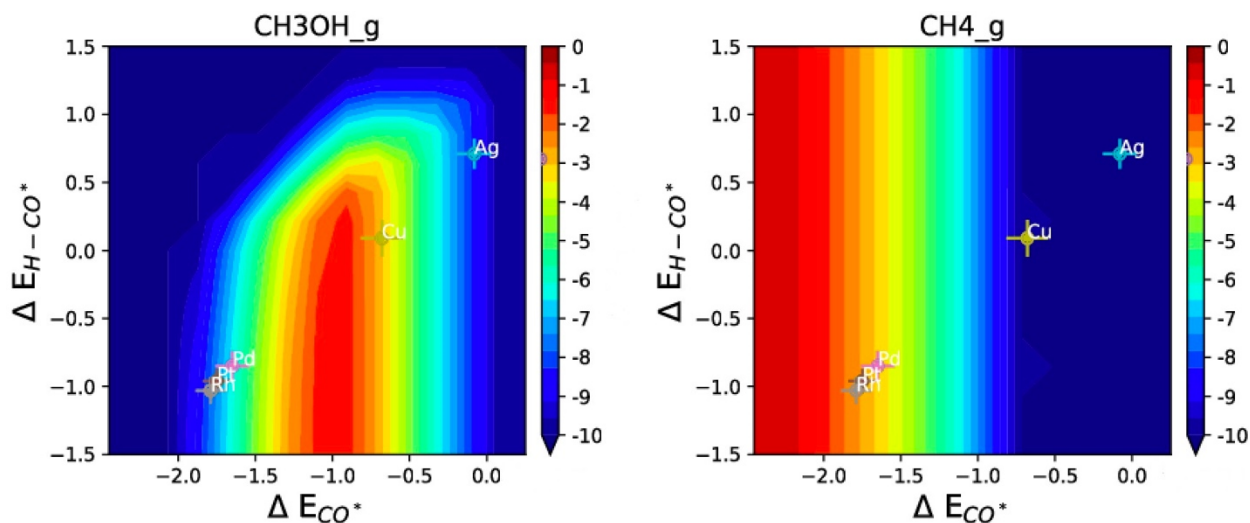


Fig. S11 Volcano plots for the rates (turnover frequency, or TOF, in s^{-1}) of methanol and methane on the (211) facets of transition metals, at $\Delta E_{OH} = -0.25$ eV, $\Delta E_O = 0.79$ eV, and $\Delta E_{CH_3O} = -1.86$ eV. The TOF is plotted against the formation energies of CO^* and the transition state $H-CO^*$. The error bars indicate the standard deviation of the BEEF ensemble calculations. The formation energies are relative to $CO(g)$, $H_2(g)$ and $H_2O(g)$

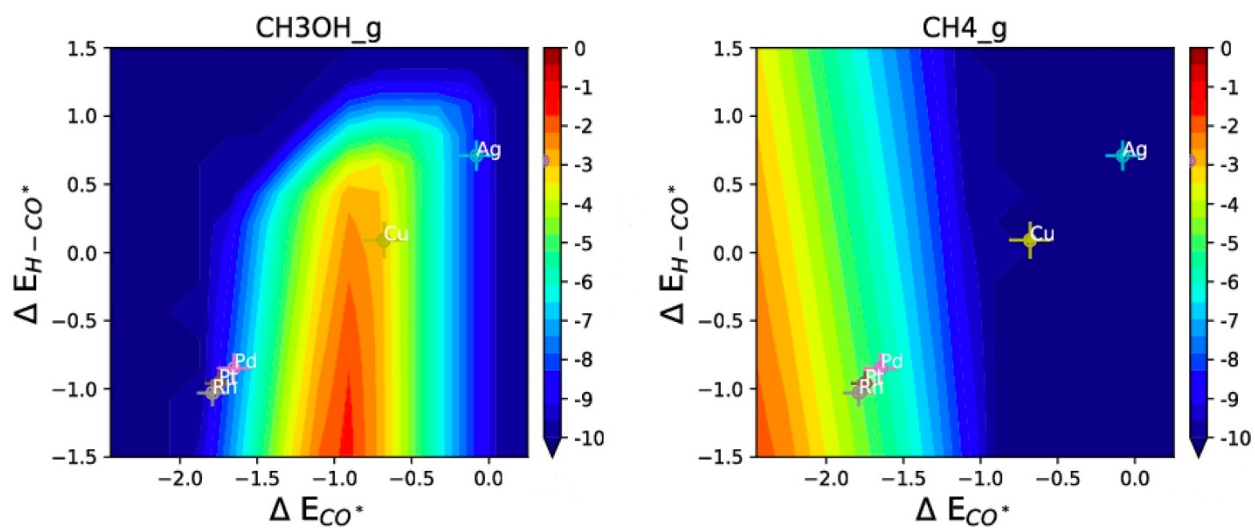


Fig. S12 Volcano plots for the rates (turnover frequency, or TOF, in s^{-1}) of methanol and methane on the (211) facets of transition metals. The TOF is plotted against the formation energies of CO^* and the transition state $H-CO^*$. The error bars indicate the standard deviation of the BEEF ensemble calculations. The formation energies are relative to $CO(g)$, $H_2(g)$ and $H_2O(g)$

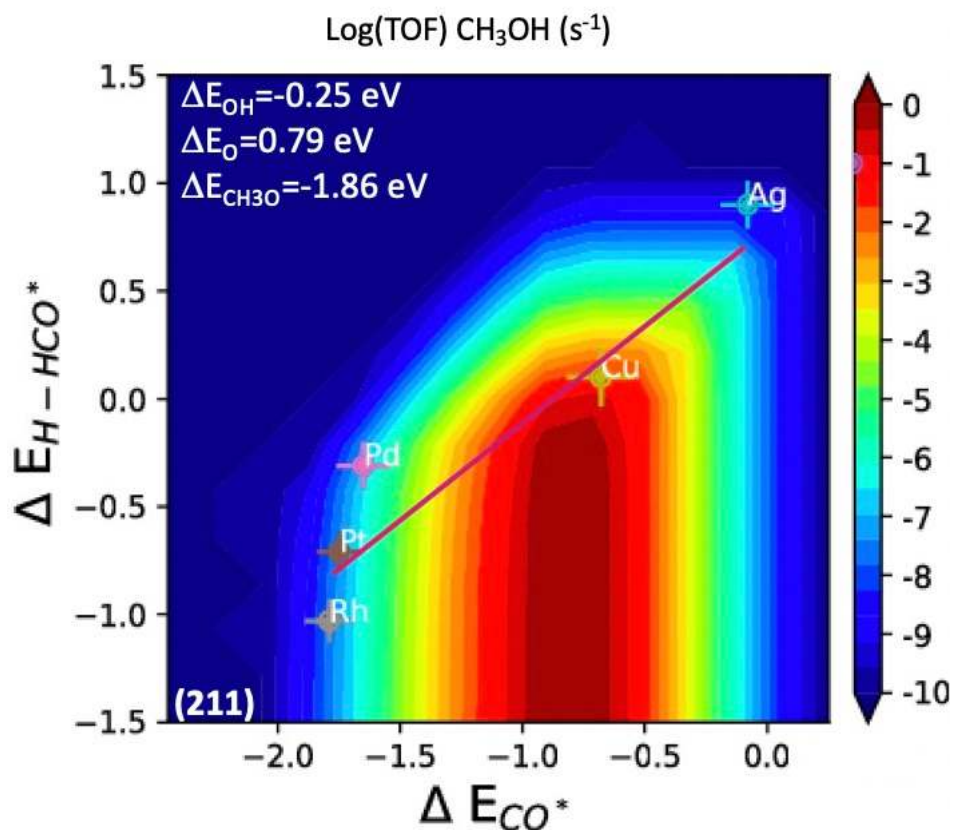


Fig. S13 Volcano plot for the rate (turnover frequency, or TOF, in s⁻¹) of methanol production via CO hydrogenation on the (211) facets of transition metals. The TOF is plotted against the formation energies of CO* and the transition state H-HCO*, allowing the superposition of the (211) linear scaling relation ($\Delta E_{\text{H-HCO}^*} = 0.93\Delta E_{\text{CO}^*} + 0.90 \text{ eV}$, $R^2=0.9073$). The error bars indicate the standard deviation of the BEEF ensemble calculations. The formation energies are relative to CO(g), H₂(g), and H₂O(g). Improved catalysis entails the stabilization of H-HCO*, without further stabilizing CO*

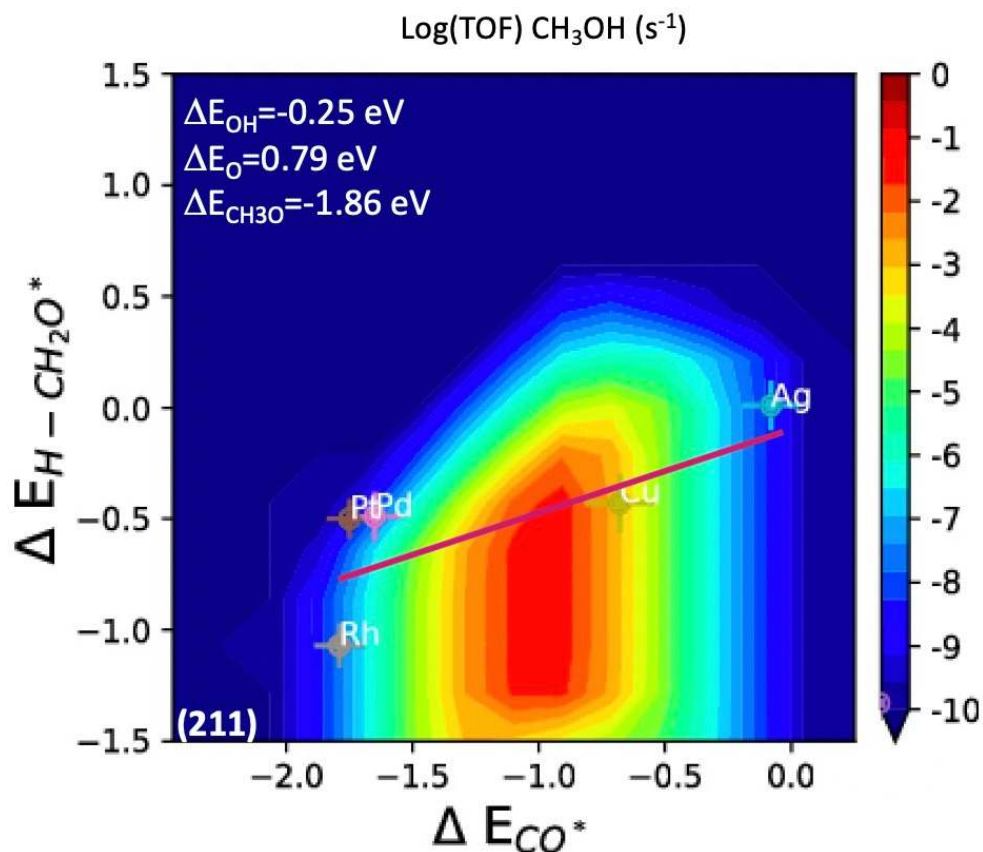


Fig. S14 Volcano plot for the rate (turnover frequency, or TOF, in s⁻¹) of methanol production via CO hydrogenation on the (211) facets of transition metals. The TOF is plotted against the formation energies of CO* and the transition state H-CH₂O*, allowing the superposition of the (211) linear scaling relation ($\Delta E_{\text{H}-\text{CH}_2\text{O}^*} = 0.40\Delta E_{\text{CO}^*} - 0.03 \text{ eV}$, $R^2=0.629$). The error bars indicate the standard deviation of the BEEF ensemble calculations. The formation energies are relative to CO(g), H₂(g), and H₂O(g). Improved catalysis entails the destabilization of CO*, without further destabilizing the transition state H-CH₂O*

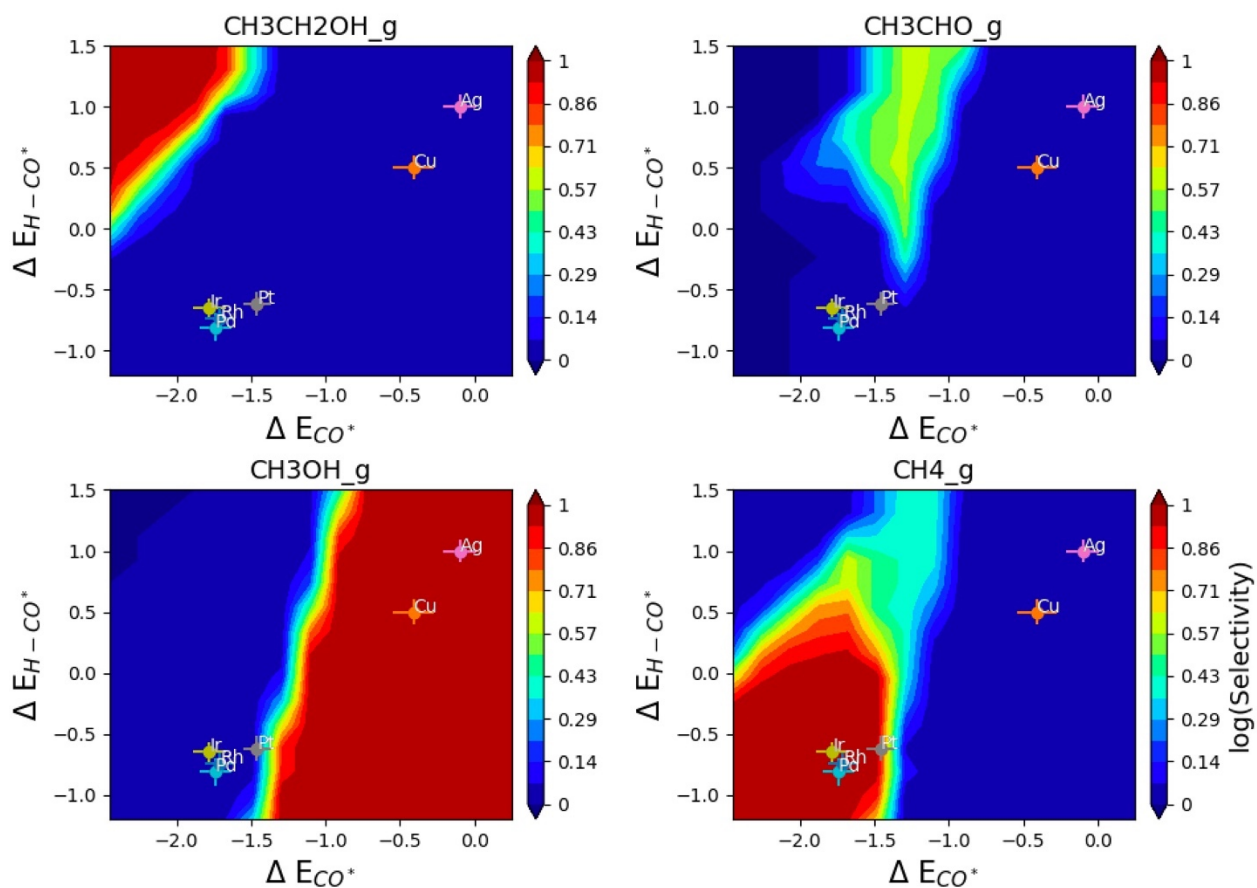


Fig. S15 Selectivity volcanoes towards C₁ and C₂ products on the (111) facets of Ag, Cu, Pt, Pd, Rh, and Ir, with the formation energies of CO* and H-CO* as descriptors. The error bars indicate the standard deviation of the BEEF ensemble calculations. Formation energies are relative to CO(g), H₂(g), and H₂O(g). Most surfaces are strongly selective towards methane, except Cu(111) and Ag(111) which are selective towards methanol

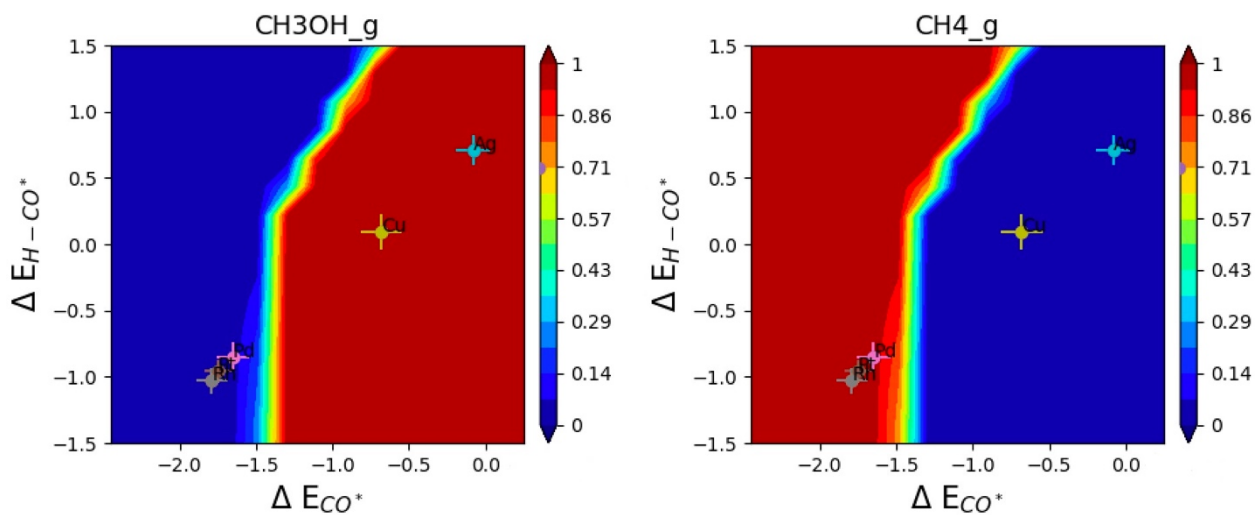


Fig. S16 Selectivity volcanoes towards methane and methanol on the (211) facets of Ag, Cu, Pt, Pd, and Rh, with the formation energies of CO^* and $H-CO^*$ as descriptors. The error bars indicate the standard deviation of the BEEF ensemble calculations. Formation energies are relative to $CO(g)$, $H_2(g)$, and $H_2O(g)$. Most surfaces are strongly selective towards methane, except $Cu(211)$ and $Ag(211)$ which are selective towards methanol

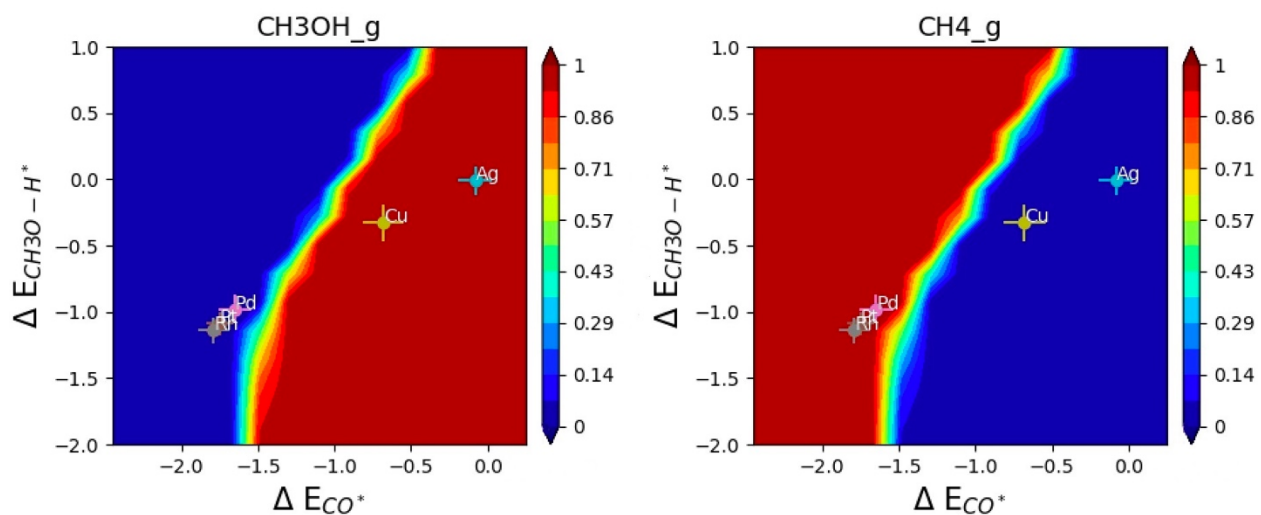


Fig. S17 Selectivity volcanoes towards methane and methanol on the (211) facets of Ag, Cu, Pt, Pd, and Rh, with the formation energies of CO^* and CH_3O-H^* as descriptors. The error bars indicate the standard deviation of the BEEF ensemble calculations. Formation energies are relative to $CO(g)$, $H_2(g)$, and $H_2O(g)$. Most surfaces are strongly selective towards methane, except Cu(211) and Ag(211) which are selective towards methanol

Table S1 DFT energies and frequencies^a on (211) transition metal surfaces

Species	Surface	ΔE_{DFT} (eV)	Frequencies (cm ⁻¹)
CO(g)	None	0.00	2170
H ₂ O(g)	None	0.00	1595, 3657, 3756
H ₂ (g)	None	0.00	4401
CH ₃ OH(g)	None	-1.55	397, 1028, 1066, 1160, 1365, 1459, 1487, 1496, 2975, 3013, 3077, 3739
CH ₄ (g)	None	-2.83	1306, 1306, 1306, 1534, 1534, 2917, 3019, 3019, 3019
H ^{*h}	Ag	0.35	
H ^{*h}	Cu	-0.06	
H ^{*h}	Pt	-0.44	
H ^{*h}	Pd	-0.30	
H ^{*h}	Rh	-0.40	237, 978, 1006
CO ^{*s}	Ag	-0.08	
CO ^{*s}	Cu	-0.68	
CO ^{*s}	Pt	-1.75	
CO ^{*s}	Pd	-1.65	
CO ^{*s}	Rh	-1.79	226, 270, 320, 362, 402, 1881
C ^{*f}	Ag	2.57	
C ^{*f}	Cu	0.75	
C ^{*f}	Pt	-0.61	
C ^{*f}	Pd	-1.26	
C ^{*f}	Rh	-1.36	303, 508, 546
OH ^{*s}	Ag	0.34	
OH ^{*s}	Cu	-0.29	
OH ^{*s}	Pt	0.22	
OH ^{*s}	Pd	0.28	
OH ^{*s}	Rh	-0.29	153, 314, 349, 650, 678, 3709
CH ^{*f}	Ag	1.46	
CH ^{*f}	Cu	0.10	
CH ^{*f}	Pt	-1.58	
CH ^{*f}	Pd	-1.24	
CH ^{*f}	Rh	-1.73	420, 428, 539, 654, 677, 2979
CH ₂ ^{*t}	Ag	0.06	
CH ₂ ^{*t}	Cu	-0.80	
CH ₂ ^{*t}	Pt	-2.07	
CH ₂ ^{*t}	Pd	-1.55	
CH ₂ ^{*t}	Rh	-1.91	52, 336, 522, 545, 577,

			762, 1299, 2978, 3081
CH ₃ ^{*t}	Ag	-1.39	
CH ₃ ^{*t}	Cu	-1.79	
CH ₃ ^{*t}	Pt	-2.45	
CH ₃ ^{*t}	Pd	-2.09	
CH ₃ ^{*t}	Rh	-2.30	12, 36, 85, 442, 594, 624, 1121, 1403, 1407, 2983, 3062, 3076
O ^{*s}	Ag	2.36	
O ^{*s}	Cu	1.12	
O ^{*s}	Pt	1.22	
O ^{*s}	Pd	1.51	
O ^{*s}	Rh	0.41	74, 477, 479
HCO ^{*s}	Ag	0.27	
HCO ^{*s}	Cu	-0.29	
HCO ^{*s}	Pt	-1.29	
HCO ^{*s}	Pd	-1.07	
HCO ^{*s}	Rh	-1.36	166, 193, 341, 367, 604, 801, 1223, 1504, 2931
CH ₂ O ^{*s}	Ag	-0.59	
CH ₂ O ^{*s}	Cu	-0.67	
CH ₂ O ^{*s}	Pt	-0.32	
CH ₂ O ^{*s}	Pd	-1.05	
CH ₂ O ^{*s}	Rh	-1.42	12, 117, 233, 312, 402, 470, 959, 1177, 1296, 1486, 2868, 2941
CH ₃ O ^{*s}	Ag	-1.20	
CH ₃ O ^{*s}	Cu	-1.85	
CH ₃ O ^{*s}	Pt	-1.44	
CH ₃ O ^{*s}	Pd	-1.36	
CH ₃ O ^{*s}	Rh	-1.94	76, 133, 157, 254, 373, 390, 977, 1141, 1148, 1451, 1465, 1471, 2963, 3030, 3036
C-OH ^{*s b}	Ag	3.24	
C-OH ^{*s b}	Cu	1.39	
C-OH ^{*s b}	Pt	0.39	
C-OH ^{*s b}	Pd	-0.33	
C-OH ^{*s b}	Rh	-0.75	102, 205, 343, 383, 421, 449, 613, 3666
H-C ^{*f}	Ag	3.40	
H-C ^{*f}	Cu	1.34	
H-C ^{*f}	Pt	0.35	
H-C ^{*f}	Pd	-0.74	
H-C ^{*f}	Rh	-0.87	157, 237, 505, 512, 1065
H-CH ^{*f}	Ag	2.34	
H-CH ^{*f}	Cu	0.89	
H-CH ^{*f}	Pt	-0.64	

H-CH ^{*f}	Pd	-0.70	
H-CH ^{*f}	Rh	-1.19	12, 380, 438, 559, 657, 895, 1573, 3012
H-CH ₂ ^{*t}	Ag	0.84	
H-CH ₂ ^{*t}	Cu	-0.43	
H-CH ₂ ^{*t}	Pt	-1.98	
H-CH ₂ ^{*t}	Pd	-1.37	
H-CH ₂ ^{*t}	Rh	-1.80	62, 278, 322, 504, 588, 852, 953, 1338, 1815, 3008, 3082
H-CH ₃ ^{*t}	Ag	-0.43	
H-CH ₃ ^{*t}	Cu	-1.14	
H-CH ₃ ^{*t}	Pt	-2.18	
H-CH ₃ ^{*t}	Pd	-2.02	
H-CH ₃ ^{*t}	Rh	-2.12	12, 156, 193, 442, 648, 657, 1073, 1219, 1320, 1376, 1416, 2642, 3026, 3096
O-H ^{*s}	Ag	3.09	
O-H ^{*s}	Cu	1.80	
O-H ^{*s}	Pt	1.88	
O-H ^{*s}	Pd	2.32	
O-H ^{*s}	Rh	1.45	12, 266, 424, 455, 1803
H-OH ^{*s}	Ag	1.90	
H-OH ^{*s}	Cu	1.18	
H-OH ^{*s}	Pt	0.59	
H-OH ^{*s}	Pd	1.11	
H-OH ^{*s}	Rh	0.57	26, 88, 348, 435, 668, 758, 1005, 3673
H-CO ^{*s}	Ag	0.71	
H-CO ^{*s}	Cu	0.09	
H-CO ^{*s}	Pt	-0.96	
H-CO ^{*s}	Pd	-0.85	
H-CO ^{*s}	Rh	-1.03	120, 197, 228, 263, 416, 548, 1671, 1823
H-HCO ^{*s}	Ag	0.90	
H-HCO ^{*s}	Cu	0.10	
H-HCO ^{*s}	Pt	-0.71	
H-HCO ^{*s}	Pd	-0.31	
H-HCO ^{*s}	Rh	-1.03	76, 216, 230, 284, 351, 587, 805, 941, 1152, 1748, 2855
H-CH ₂ O ^{*s}	Ag	0.01	
H-CH ₂ O ^{*s}	Cu	-0.43	
H-CH ₂ O ^{*s}	Pt	-0.50	
H-CH ₂ O ^{*s}	Pd	-0.49	
H-CH ₂ O ^{*s}	Rh	-1.07	12, 146, 170, 209, 332, 535, 664, 1087, 1185, 1339, 1514, 1587, 2928, 2982
CH ₃ O-H ^{*s}	Ag	-0.01	

CH ₃ O-H ^{*s}	Cu	-0.33	
CH ₃ O-H ^{*s}	Pt	-1.09	
CH ₃ O-H ^{*s}	Pd	-0.98	
CH ₃ O-H ^{*s}	Rh	-1.14	56, 91, 127, 199, 227, 289, 568, 837, 998, 1126, 1146, 1397, 1467, 1480, 2951, 2976, 2996

^a Frequencies have been calculated on Rh(211) and previously reported in N. Yang, A. J. Medford, X. Liu, F. Studt, T. Bligaard, S. F. Bent, J. K. Nørskov, *J. Am. Chem. Soc.* **2016**, 138, 3705-3714.

^b Calculated on surfaces with steps covered with CO at 2/3 ML coverage of CO spectators. Both spectator CO molecules occupy the bridge sites on the step edge.

Table S2 Calculated entropy for H-CO* and the TS term at 300, 500, and 600 K

T (K)	S _{TS} (eV/K)		TS _{TS} (eV)	
	(111)	(211)	(111)	(211)
300	0.0004074	0.0004477	0.122	0.134
500	0.0006234	0.0006887	0.312	0.344
600	0.0007130	0.0007844	0.428	0.471

Table S3 Entropies of gas-phase CO and H₂ at 300, 500, and 600 K, as obtained from janaf.nist.gov

T (K)	S (eV/K)		TS (eV)	
	CO (g)	H ₂ (g)	CO (g)	H ₂ (g)
300	0.00205	0.00136	0.61512	0.40688
500	0.00221	0.00151	1.10292	0.75523
600	0.00226	0.00157	1.35763	0.93948

Table S4 Entropies of H-CO* relative to CO(g)+1/2H₂(g) at 300, 500, and 600 K. Entries at a given temperature are calculated by subtracting the corresponding TS entry from Table S2 and the corresponding TS entries for CO+1/2H₂ from Table S3

T (K)	TΔS _{TS} (eV)	
	(111)	(211)
300	-0.696	-0.684
500	-1.169	-1.136
600	-1.400	-1.357